Title
THE LOW TEMPERATURE BRITTLE FRACTURE OF AUSTENITIC Fe-Mn ALLOYS

Author
Xue, K.-S.

Publication Date
1986-05-01

LBL-20938

THE LOW TEMPERATURE BRITTLE FRACTURE OF AUSTENITIC Fe-Mn ALLOYS

K.-S. Xue
(M.S. Thesis)

May 1986

Lawrence Berkeley Laboratory
University of California
Berkeley, California 94720

Prepared for the U.S. Department of Energy
under Contract DE-AC03-76SF00098

Center for Advanced Materials

DISCLAIMER

THE LOW TEMPERATURE BRITTLE FRACTURE OF AUSTENITIC Fe-Mn ALLOYS

by

Kan-Shi Xue
M.S. Thesis

University of California
Lawrence Berkeley Laboratory
Berkeley, California 94720

May, 1986

TABLE OF CONTENTS

ABSTRACT

Austenitic chromium-nickel stainless steels, such as 304 and 316, have been widely used in a variety of cryogenic applications. However, in recent years it has been recognized that there is a great need for developing new cryogenic steels to substitute Ni-Cr austenitic steels. Manganese is the most obviously attractive as a substitute for nickel in cryogenic alloys. However, face-centered cubic high manganese steels, differ from most other fcc metals, which do not undergo a ductile-to-brittle transition. High manganese steels still exhibit the ductile-to-brittle transition. The mechanism of low temperature brittleness of high manganese steels is not clear. The purpose of this investigation was to determine the metallurgical source for the low-temperature brittleness of austenitic Fe-Mn alloys.

The ductile-to-brittle transition of high manganese austenitic Fe-Mn alloys is accompanied by a change in the fracture mechanism from micro-void coalescence to intergranular fracture. No impurity element segregated to grain boundaries was found. The results of AES analyses indicate that manganese segregates to the grain boundaries. The magnitude and extent of manganese segregation to grain boundaries increases with increasing manganese content. The manganese segregation is a kind of non-equilibrium segregation. Increasing solid-solution treatment temperature and the following cooling rate, the manganese segregation to the grain boundaries is increased. Increasing the manganese content of Fe-Mn alloys, solid-solution treatment temperature and the following cooling rate, the ductile-to-brittle transition temperature and intergranular fracture are increased. These results indicate that the intergranular

fracture and embrittlement of high manganese austenitic Fe-Mn alloys at low temperature are caused by manganese segregation. The possible mechanism for intergranular fracture of these alloys and the way to improve low-temperature toughness of high manganese steels are discussed.

ACKNOWLEDGEMENTS

I wish to sincerely thank Professor J. W. Morris, Jr. for his support and guidance throughout this investigation. I am also grateful to Professor R. O. Ritchie and Professor R. M. Fisher for their reviews and comments on this thesis.

I would like to thank Dr. Lenny Summers and Professor Brent Fultz for their productive discussions. I would also like to extend my thanks to the members of the Morris' research group, especially Darrel Frear, Gee-Minn Changm, Michael Strum and Ze-Qun Mei for their help.

My thanks go to the technical staff for their assistance on this project, to Jeanne Shull for her careful assistance in preparing this manuscript, to Gloria Pelatowski for most of the line drawings, to John Holthuis, John Jacobson and Harvey Sokol for the preparation of materials, to Wayland Wong and Herb Riebe for preparation of specimens, and to Ken Gaugler for his assistance with the AES work.

My warmest gratitude is to my family, especially my parents, my wife, Min-chun, my godmother, Mrs. C. B. Sawyer, and also to my friend, Jenny Shen, for their unconditional support and continuous encouragement.

This work was supported by the Director, Office of Basic Energy Science, Material Science Division of the U.S. Dept. of Energy under contract number DE-AC03-76SF00098.

I. INTRODUCTION

One of the basic requirements for steels used in cryogenic technology is that they retain toughness at operating temperature. The toughness of the steel determines the working capacity and safety of the equipment.

Toughness is usually decreased as temperature is lowered. There is characteristically no ductile-to-brittle transition in face-centered cubic metals. Fcc metals have excellent ductility at room temperature and remain ductile at low temperature. The toughness of Ni-Cr austenitic steels are decreased gradually as the temperature is lowered; however, they still retain sufficient toughness at low temperature. The ductile-to-brittle transition does not normally occur in the Ni-Cr austenitic steels; therefore, the Ni-Cr austenitic steels, such as 304 and 316, have been widely used in a variety of cryogenic applications.

In recent years, it has been recognized that there is a great need for developing new cryogenic steels to substitute for the Ni-Cr austenitic steels. The reasons are:

1. The operation temperature of cryogenic devices was extended to liquid helium temperature. The 304 stainless steel is unstable at 4 K. Some austenite transform to martensite and influence the toughness and magnetic properties;

2. Increasing the nickel content increases the stability of austenite but may change magnetic properties;

3. Nickel is expensive.

Manganese is the most obviously attractive substitute for nickel in cryogenic alloys. Manganese is readily available, relatively inexpensive and has a metallurgical similarity to nickel in its effect on the microstructures and phase relationships of iron-base alloys. Many high manganese austenitic cryogenic steels were developed [1-16].

Face-centered cubic high manganese steel differs from most other fcc materials in that they undergo a ductile-to-brittle transition. Some Cr-Mn-N steels transform to martensite during deformation [17-21], and several investigators [17-19,22,23] have suggested that the brittle behavior of these steels is caused by martensite formation. However, very stable Cr-Mn-N steels also exhibit brittle behavior. Schaller and Zackay [17] reported that a very stable Cr-Mn-N steel (less than 0.5% martensite formed at -320°F) exhibited a transition temperature higher than that for steels in which large volume fractions of martensite formed during testing. The explanation given by Schaller and Zackey for this was that in the very stable steel, the martensite was more brittle than that formed in their other steels due to its higher interstitial content. This explanation does not account for Thompson's [24] observation that small additions of nickel (1 to 3%) greatly improve the toughness of high nitrogen (0.35%) Cr-Mn-N steels.

The research work of high interstitial content austenitic Cr-Mn-N steel by Tisinai and Samans [20] indicated that the impact transition was accompanied by a change from a high ductility shear fracture to a low ductility intergranular fracture.

The research work on the low-temperature brittleness in very stable Cr-Mn-N steels [25] has shown that transformation to martensite probably

is not the principal cause of the embrittlement of stable austenitic Cr-Mn-N stainless steels even though this transformation has been shown to be the cause of embrittlement of metastable Cr-Mn-N steels. Breedis [26] has shown that the tendency for faulting in fcc steels increases as the temperature of deformation decreases. It is quite possible that during high strain-rate deformation of stable austenitic Cr-Mn-N steels, faulting can become an important deformation mode. The high local shear associated with the faults could cause the fracture strain to be exceeded in the vicinity of the faults. The resultant crack could possibly propagate catastrophically under the existing state of stress before the energy of deformation could be absorbed by other parts of a specimen. Defilippi, et al. [25] pointed out that the deformation faulting is a possible mechanism of brittle failure in the stable austenitic Cr-Mn-N stainless steels because stacking faults persist in these steels during deformation, especially low-temperature deformation.

An implication of the deformation-faulting mechanism is that the toughness of high-strength Cr-Mn-N steels should improve as the stacking fault energy of these steels increases.

The research work of Suto and Chun [27] has shown that the fracture mode of high-carbon, high-manganese steel is ductile dimple at -76°C, but brittle intergranular fracture occurred at liquid nitrogen temperature. It was also considered that the intergranular brittle fracture at low temperature was caused by the segregation of impurities (P,S,Sn, etc.) segregations to grain boundaries. A high purity high-carbon, high-manganese steel was prepared. It was diffusion annealed and water quenched from 1050°C, but the low temperature toughness was not improved

at all by the purification. Gulyaev has reported the same results [28]. Three basic types of fracture were observed, depending on the testing temperature and the phosphorous content of the steel. The first is trans-crystalline fracture in the form of dimples of different sizes. This type of fracture is observed in specimens tested at room temperature and corresponds to ductile fracture. The second type is intercrystalline in the form of sections with an undulating topography. The third type is intercrystalline fracture in the form of flat surface. Slip lines were observed on the flat sections. This type of fracture is brittle. It is typical of tests at low temperatures and is associated with very low values of impact toughness. Even when the phosphorous content is very low (<0.001%P) the toughness is low at low temperature. Martensite is not formed in any case. From these facts, it was concluded that the intergranular fracture at low temperature of high carbon and high manganese steel was an "intrinsic" behavior of this alloy.

Gylyaw and Volynova [29] have determined the ductile characteristics, type of fracture, and the characteristics of resistance to ductile and brittle fracture of binary Fe-Mn alloys. Alloys of exceptionally high purity are obtained by using modern metallurgical methods. With ≥29% Mn the γ phase is stable at room temperature. Impact tests lead to formation of some quantity of ε phase in alloys with 29 and 35% Mn. The quantity of the ε phase formed is identical (10%) in the alloy with 29% Mn at all testing temperatures, while the amount of the ε phase formed decreases with the testing temperature in alloys with 35% Mn. No ε phase is formed in alloys with 40-45% Mn in impact tests at any temperature. Therefore, changes in the ductile-brittle transition tempera-

ture are not due to the formation of the ε phase. In austenitic alloys (29-54% Mn) manganese raises the ductile-brittle temperature. For alloys with 35-54% Mn a ductile-brittle transition is clearly visible. In the ductile range the fracture is completely dimpled and in the brittle range it is intergranular.

Namekata and Kondo [30] reported the same results as Gulyaev and Volynova, i.e., the transition temperature of stable austenitic Fe-Mn alloys are increased as the manganese content are increased. They also reported that a few percent addition of Cr and Ni improve low temperature brittleness of γ-single phase steels.

The mechanism of low temperature brittleness of high manganese steels is not clear. The purpose of this work was to determine the reason for the low-temperature brittleness of austenitic Fe-Mn alloys.

II. EXPERIMENTAL PROCEDURES

A. Materials Preparation.

The alloy used in this investigation was prepared in a Temescal 125 KV vacuum induction furnace. The elements used were high purity (99.9+%) iron and manganese and were melted in magnesium oxide crucibles, first under a vacuum at 10^{-3} mm Hg and then under argon atmosphere. From this melt 2.4 inch (61 mm) diameter ingots were cast in copper chill molds and cooled in an argon atmosphere. The ingots were homogenized for twenty-four hours at 1200°C in an argon atmosphere and then the ingots were furnace cooled. The homogenized ingots were hot rolled at 1200°C in air to a cross section of 16 mm (5/8 in.) then air cooled.

The compositions and designations of the alloys are listed in Table I.

B. Heat Treatment.

After forging, the bars, which were protected by stainless steel bags, were austenitized at 1000°C for one hour in air followed by agitated quenching in an ice brine bath. During the quenching process, the stainless steel bags were torn off. The test specimens are machined from the plate after heat treating. The heat treatment of specimens used for studying the effects of austenitizing temperature and cooling rate are described later.

C. Mechanical Tests.

1. Charpy impact test.

The Charpy impact test specimens were machined from solution-treated steel plate to ASTM standard size shown in Figure 1. Notches of

45° were machined perpendicular to the rolling direction of the plate and through the thickness of the plate, i.e., thickness direction. The impact tests were carried out as described in ASTM E23. Various temperatures were obtained by a proper mixture of liquid nitrogen and isopentane. At least two Charpy V-notched specimens were tested at each testing temperature.

2. Tensile test.

Round tensile specimens of 1/2 in (12.7 mm) in diameter were machined from solution-treated steel plate to the ASTM standard size shown in Figure 2. Tensile tests were carried out on a 6000 kg capacity Tinius Olsen testing machine at a crosshead speed of 4 mm/min at liquid nitrogen temperature. The 0.2% offset method of determining the yield stress was used. Two specimens of each composition were broken to determine the mechanical properties of these Fe-Mn alloys. Two specimens of each composition were unloaded at maximum load to determine the true stress and uniform reduction area at the maximum load. The strain hardening exponents were determined according to ASTM E646-78.

D. X-ray Diffraction.

X-ray diffraction analyses were carried out on specimens cut from broken Charpy specimens along the longitudinal direction. Specimen surfaces were carefully ground on emery paper to 600 grade and chemically polished in a solution of 100 ml H_2O_2 + 3 ml HF for 15 minutes in order to remove any strain-induced transformation phases from previous grinding processes. Once polished, these specimens were scanned in a Siemens Kristalloflex X-Ray diffractometer using Cu Kα radiation. The volume percent of each phase was calculated by comparing average integrated

intensities of $(101)_\varepsilon$ and $(200)_\gamma$. The formula [31] used was:

$$V_\varepsilon = \frac{1}{1 + \frac{R_\varepsilon}{R_\gamma} \cdot \frac{I_\gamma}{I_\varepsilon}} = \frac{1}{1 + 1.97 \frac{I_{(200)\gamma}}{I_{(101)}}}$$

E. Microscopy.

1. Optical microscopy.

Optical metallography was conducted on a Carl Zeiss Universal Photomicroscope Ultraphoto II. Specimens for optical microscopy were cut from the broken Charpy impact specimens along the longitudinal direction. They were wet ground on successive emery papers up to 600 grade. The specimens were then mechanically polished on 6 and 1 μm (micron) diamond paste wheels lubricated with kerosene, followed by ultrasonic cleaning. Etching was accomplished using Vilella's reagent which contains 5 ml HCl, 1 gm preric acid and 100 ml ethanol (95%).

2. Scanning electron microscopy (SEM)

The fracture surfaces of broken Charpy specimens were examined with a ISI-DS130 scanning electron microscopy operated at 20 kv.

F. Auger Electron Spectroscopy (AES).

Specimens for Auger electron spectroscopic (AES) studies were machined from solution-treated steel plate. The shape and size of the Auger specimens are illustrated in Figure 3.

The Auger electron spectroscopic studies were carried out with a PHI model 590 scanning Auger microscopy (SAM) combined with a scanning electron microscope and an Ar^+ ion sputtering gun. The specimen was put into the reaction chamber equipped with an in-situ fracturing and cooling stage, shown in Figure 4. The temperature of the specimens inside the reaction chamber was controlled by liquid nitrogen flowing through

the fracture stage, monitored by a thermocouple. The specimen was cooled to between -156 to -158°C within 30 minutes. The specimens to be fractured were subjected to a 5×10^{-10} - 1×10^{-9} Torr vacuum attained by employing a differential ion pump, a Ti sublimation pump and a liquid nitrogen cold trap. The specimens were fractured by hammer to reveal the fresh fracture surface.

After fracture, the specimen was positioned in front of the SAM cylindrical mirror analyzer (CMA). The primary exciting electron beam energy and beam current used were 5 KeV and 0.8-1μA, respectively. The primaryelectron beam size ranging 0.5-2μm in diameter was regulated according to the place needed to be analyzed. In order to obtain a typical spectrum from a grain boundary, at least 7 points on an intergranular fracture surface were analyzed with 0.6% (i.e. $\pm$ 0.3%) energy resolution, monitored by the attached scanning electron microscope. The amplitude of the modulation voltage was 4 eV. The multiplier gain was 10^3 in general use. The sensitivity setting of the lock-in amplifier was 10-20X. The time constant per point and sweep rate were 0.03 second and 33 eV/sec, respectively.

Following the AES analysis on the fresh fracture surface, the surface was sputtered by an Ar^+ ion gun at normal incidence. In most cases, a primary ion beam voltage of 4 kV was used. The sputtered area on the fracture surface was 2 x 2 mm. The sputtering rate of Mn-Fe alloy approximately 50 Å/min. The sputtered regions were reanalyzed to compare the difference between the surface before and after sputtering.

Intergranular surface chemical composition was calculated from the Auger peak-to-peak amplitudes on the AES spectra of the specimen frac-

tured in an ultra high vacuum. The atomic percent C_X of element X is approximated by

$$C_x = \frac{\frac{I_x}{S_x d_x}}{\Sigma_n \frac{I_n}{S_n d_1}}$$

where I_x us the peak-to-peak Auger amplitude, S_x is the relative sensitivity between element x and the standard, and d_x is the scale factor which is $L_x E_{m,x} I_{p,x}$. The scale factor d_x in this equation is constant if the lock-in amplifier sensitivity, L_x, modulation, $E_{m,x}$, and the primary beam current, $I_{p,x}$ setting used to obtain the test spectrum are the same for all peaks and cancel out.

III. EXPERIMENTAL RESULTS

A. Charpy Impact Test.

Charpy impact tests were performed to determine the fracture behavior of various Fe-Mn alloys. The results of these tests are shown in Fig. 5. The upper shelf energies at 20°C are almost the same for these Fe-Mn alloys. The toughness of these Fe-Mn alloys is decreased as the test temperature decreases. These face-centered-cubic Fe-Mn alloys differ from most other fcc alloys, which undergo a ductile-to-brittle transition. A ductile-brittle transition is clearly visible for these alloys on the fracture toughness curves, as shown in Fig. 5. In these austenite manganese alloys, manganese raises the ductile-to-brittle transition. As shown below, (paragraph D) the ductile-to-brittle transition is accompanied by a fracture mode transition that is changed from a dimple mode to an intergranular fracture mode at low temperature. From a practical viewpoint, even in the worst condition, i.e., 45 Mn alloy at liquid nitrogen temperature, the impact toughness is not very low.

B. Tensile Test.

Tensile tests were carried out to determine the mechanical behavior of these austenitic Fe-Mn alloys. The results are shown in Table 2. The tensile curves are shown in Figs. 6 to 8. The yield strength and ultimate tensile strength of different Fe-Mn alloys are almost the same. The strain hardening characteristics are correlated with the stacking fault energy [32]. When the stacking fault energy is low, cross-slip is restricted so that barriers to dislocation movement remain effective to higher stress levels than that of higher stacking fault energy. That is

to say, there is increased strain hardening exponent with decreasing stacking fault energy. Manganese is known to significantly lower the stacking fault energy [33,34]. The results shown in Table 2 confirm that the strain hardening exponent increases with increasing manganese content. The uniform plastic deformation, total plastic deformation, and true stress at maximum load increase with the increase of manganese content due to the increase of strain hardening exponent. As a result of the higher inclusion content, the 40% Mn alloy has a lower value of total plastic deformation.

C. X-Ray Diffraction.

Manganese increases the stability of austenite [1,29]. The (Fe-Mn) alloys tested are fully austenitic at room temperature. The results of X-ray diffraction tests listed in Table 3 show that the microstructure of specimens cooled down to 77 K are fully austenitic. Even when deformed at 77 K, all the alloys are fully austenitic except for the 35 Mn alloy which has approximately 2% ε. These results are in agreement with those reported by Gulyaev and Volynova [2] and Tomota [29].

D. Scanning Electron Microscopy (SEM).

As the testing temperature of the impact test is lowered from high temperatures to very low temperatures, the fracture mechanism of the austenitic Fe-Mn changes from micro-void coalescence to intergranular fracture,as shown in Figs.9 to 14. The fracture surfaces of the 35 Mn alloy specimen fractured at -102°C, exhibiting dimple mode fracture that was formed by microvoid coalescence. The fracture features of the 35 Mn specimen broken at -196°C are ductile fracture plus some intergranular

fracture. Inclusions exist in the dimples. The inclusions were analyzed in the SAM and were determined to be MnS(O).

The fracture surfaces of the 40 Mn specimen fractured at -102°C are a mixed mode of dimple and intergranular fracture but most of them are dimple fracture. Some slip line traces exist on the intergranular fracture surface, as shown in Fig. 11b. This indicates that plastic deformation had occurred before fracture along the grain boundary. For specimens fractured at -196°C, the fracture surfaces consist of intergranular fracture and a small amount of dimple fracture. The traces of plastic deformation are still observed on the intergranular fracture surface, as shown in Fig. 12b.

For the 45 Mn alloy, the fracture surfaces of the specimen fractured at -102°C exhibit a mixed mode of dimple fracture and intergranular fracture. For specimens fractured at -196°C, the fractography shows that the major fractures are intergranular and contain a small amount of dimple fracture, as shown in Fig. 14. Although the plastic deformation traces still exist on the intergranular fracture surface, the intergranular fracture surfaces are smoother than in the 40 Mn alloy. This indicatesthat the plastic deformation before fracture is less thanin40 Mn.

E. Auger Electron Spectroscopy (AES).

Chemical analyses of the intergranular fracture surfaces of the Fe-Mn alloys were obtained by using a high resolution scanning Auger microscope. The Auger electron spectra obtained from the <u>in-situ</u> fracture surfaces of the alloys in the as-austenitized condition are shown in Figs. 15 to 17, together with the corresponding SEM fractograph. The

surface-sensitive AES technique [36-40] was applied to detect any segregation within a monolayer of the surface on the austenite grain boundaries, i.e., the fracture path of these alloys.

Manganese segregation was investigated by use of the Ar^+ ion sputtering technique. Manganese has four different major Auger electron transition peaks that are the KLL Auger transition peak at 40 eV, and the LMM peaks at 542 eV, 589 eV, and 636 eV, respectively. Since the strongest Mn Auger elect peak at 589 eV is very close to the strong Fe Auger peak at 598 eV, the Mn peak at 542 eV was used to obtain the Mn depth profile.

The chemical composition of the grain boundary is determined by AES on the intergranular fracture surface before Ar^+ ion sputtering. The chemical composition of the grain was obtained from the Ar^+ ion-sputtered surface after sputtering for 10 minutes. Therefore the magnitude of the element segregation at the grain boundary can be determined by the difference of composition determined before and after sputtering.

Much of the research work [41-44] reported that segregation of residual elements, such as S, P, As, Sn, Sb and Bi, on the grain boundary often causes intergranular fracture. From Figs. 18 to 20, it can be seen that there are no such residual elements segregated on the grain boundary. Therefore, the intergranular fracture of austenitic Fe-Mn alloys appears not to becaused by the segregation of such residual elements.

Also, it can be seen from Figs.15 to 17 that the peak-to-peak heights of the Mn 542 and the Fe 598 peaks are changed after sputtering 10 minutes. It clearly indicates that manganese segregates at the grain

boundary. The manganese content of the grain boundary and the interior of the grain for 35 Mn, 40 Mn and 45 Mn alloys are plotted in Fig. 21. This diagram shows the mangenese segregation at the grain boundary. Figure 19 shows the linear relationship between the manganese content of the grain boundary and the interior of grain. Figure 20 indicates that the magnitude of manganese segregation at the grain boundary (ΔMn) is increased with the increasing manganese content of Fe-Mn alloys.

The manganese depth profiles of Fe-Mn alloys are shown in Figs. 21 to 22. From these curves, the thickness of manganese segregation zone can be determined. Figure 23 presents the thickness of manganese segregation zone of three Fe-Mn alloys. It indicates that the thickness of manganese segregation zone is increased with increasing manganese content of the Fe-Mn alloys. The influences of magnitude and thickness of the manganese segregation to grain boundaries on the toughness of Fe-Mn alloys are shown in Figs. 24 and 25.

F. Effects of Austenitizing Temperature and Cooling Rate.

In order to observe the effect of austenitizing temperature on the segregation of manganese at the grain boundary, samples of 45 Mn were heat-treated by three different heat-treatment processes. These heat-treatment processes are schematically shown in Fig. 26. In order to get the same austenite grain size, all specimen blanks are heated to 1150^{o}C for 1 hr. One blank was quenched directly from 1150^{o}C into ice brine. A second blank was transfered from the 1150^{o}C furnace to a 1000^{o}C furnace and quenched in ice brine after holding for 1 hr at 1000^{o}C. The third blank was transferred from the 1150^{o}C furnace to a 850^{o}C furnace and quenched in ice brine after holding 1 hr at 850^{o}C. The Charpy

impact toughness of specimens heat treated by these three heat treatments are shown in Fig. 27 and it can be seen that the impact toughness is decreased with increasing austenitized temperature.

The Auger electron spectra obtained from these specimens are shown in Figs. 28 to 30. Figure 31 shows the effect of austenitizing temperature on the manganese concentration at the grain boundary. It indicates that the austenitizing temperature has very little effect on manganese concentration at the grain boundary; however, austenitizing temperature does have an effect on thickness of the manganese segregation zone, as shown in Fig. 32. The thickness of manganese segregation zone is increased with increasing austenitizing temperature.

To study the effect of cooling rate in the austenitizing treatment on the manganese segregation, one specimen blank was air cooled and another specimen blank was furnace cooled after heating to 1000°C and holding 1 hr. The Auger electron spectra obtained from these specimens are shown in Figs. 33 and 34. In Figs. 35 and 36, it can be seen that the manganese concentration at the grain boundary and the thickness of manganese segregation zone is decreased with decreasing cooling rate. Comparing the fractographs for slowly cooled Auger specimens shown in Figs. 33 and 34 with the fractograph of the fast quenched specimen shown in Fig.17, it can be seen that the alloy is tougher in the slow cooling condition than in the fast one.

DISCUSSION

For a long time it has been known that high manganese austenitic steel exhibits a ductile-to-brittle transition phenomenon in impact tests [17-19,22,23,25,27]. The materials used in many earlier research investigations have phase transformations or precipitates, but the research work done in recent years has shown that even simple and very stable austenitic Fe-Mn alloys also exhibit a ductile-to-brittle transition [29,30]. Furthermore, even high manganese austenitic alloys with very high purity show a brittle transition [27,29]. Therefore, the ductile-to-brittle transition behavior is an "intrinsic" behavior of high manganese austenitic alloys, but the metallurgical source of this behavior is not clear. Therefore, the materials that were used in this research were simple and very stable austenitic Fe-Mn alloys in order to avoid the influence of phase transformation, precipitates and other alloying elements.

The results obtained from X-ray diffraction tests show the Fe-Mn alloys containing 35% Mn, 40% Mn and 45% Mn, which were used in this investigation, are very stable at 77 K. Even after deformation at 77 K, only approximately 2% ε phase was found in the 35% Mn alloy and no ε was found in 40% and 45% Mn alloys. This is in accord with the results of Gulyaev and Volynova [29] and Tomota [35]. The impact toughness test reveals a ductile-to-brittle transition. This is also in agreement with the results reported by Gulyaev and Volynova [29] and Namekata and Kondo [30]. The transition temperature is increased on increasing the manganese content.

The low stacking fault energy material has a high strain hardening exponent. The strain hardening exponent increases with decreasing stacking fault energy while the slip character changes from a wavy to planar mode. Tamura [33] and Dulieu and Nutting [34] reported that stacking fault energy decreases with increasing manganese content. The strain hardening exponent therefore should increase with increasing manganese content. The results obtained in this investigation confirms this point as shown in Table 2.

The yield strength and ultimate tensile strength of different Fe-Mn alloys are almost the same. The uniform plastic deformation, total plastic deformation and true stress at maximum load increases with increasing manganese content. Large uniform elongations can be achieved since local deformation can be prevented. If a local deformation neck starts to develop in the middle of gage length, further deformation would be prevented by hardening due to high strain hardening exponent. Necking could then start at other regions but would similarly again be prevented. The resultant multiple necking mechanism yields the high uniform elongations.

The appearance of a ductile-to-brittle transition in the fracture behavior of stable austenitic high manganese alloys is accompanied by a change in the fracture mechanism from microvoid coalescence to intergranular fracture. In the upper shelf region, the fracture forms in a dimple mode caused by microvoid coalescence. The upper shelf energies are almost the same for these three Fe-Mn alloys. On decreasing the test temperature, the fracture mechanism change from microvoid coalescence to intergranular fracture.

In general, the intergranular fracture in ferrous alloys in non-aggressive environments can be classified into two general categories: those owing to the presence of certain grain boundary phases and those owing to thermal treatment that cause segregation of certain impurities to the grain boundaries without an observable second phase [41,46,47]. The intergranular failure owing to the presence of a grain boundary phase is also called "intergranular rupture". This type of intergranular failure is caused by the presence of a well-defined second phase at the grain boundaries. The phase is almost always particulate rather than continuous, although it may cover well over 50% of the grain boundary area. In most instances where such particles cause intergranular failure, small cavities form around the grain boundary precipitates. The growth of these cavities and their eventual link-up cause the crack to proceed along the grain boundaries. It has been pointed out that intergranular fracture surfaces produced in this manner are not the smooth "rock candy" surface, rather, many small dimples in microscopic scale appear on the intergranular fracture surface.

The presence of certain residual elements at the grain boundaries of materials is one of the major causes of intergranular fracture. These elements are believed to lower the cohesive energy of the boundaries and, at a given concentration, they can change the brittle-fracture path from the cleavage plane to the grain boundaries. The most common grain boundary embrittlers are from groups IV to VI in the periodic table, e.g., Sn, P, As Sb, Bi and S. In this case, the intergranular fracture surface is smooth "rock candy" surface.

The intergranular fracture surface of high manganese austenitic Fe-Mn alloys is different from the two kinds of intergranular fracture surfaces mentioned above. Traces of plastic deformation exist on the intergranular fracture surface as can be seen from Figs. 10 to 14 Especially in the high magnification fractograph shown in Fig. 11b where some trace of the slip line exists on the intergranular surface. This indicates that plastic deformation had occurred before fracture along the grain boundary. This is the reason that even when the major of the fracture surfaces are intergranular fracture as shown in Figs. 12 and 14, the impact toughness is still not very low, and higher than the toughness requirement of the industrial standard. The difference between the fracture surface of high manganese alloys and those associated with the two kinds of intergranular fracture mentioned above also indicates that the intergranular fracture mechanism is different.

Some parallel small lips or "tongues" protrude from the fracture surface (Shown in the left part of the fractograph shown in Fig. 11b). Berry [48] has explained that the tongues form when a cleavage crack propagating along the (100) plane interacts with a mechanical twin produced by the stress field ahead of the running crack. During this interaction, the crack path can propagate along the (112) twin plane for a short distance before it continues again along the (100) cleavage plane. The result of this interaction is the formations of tongues that protrude in a (112) direction from the (100) cleavage surface.

Analogous to Berry's arguments, the tongues on fracture surface shown in Fig. 11b may be caused by the interaction of the intergranular fracture path with stacking fault formed near the grain boundary. Due

to high manganese concentration and low stacking fault energy in the manganese segregation zone at the grain boundary, stacking faults tend to form at this region. A crack propagating along the grain boundary could interact with the bands of stacking faults that form on the (111) planes near the grain boundary. Tongues would form as a result of the propagating crack following the intersecting (111) planes for short distances.

The AES technique was applied to detect any segregation within a monolayer of the surface on the prior austenite grain boundaries. After AES analysis of the in-situ fractured surface, Ar+ ion-sputtering technique was employed. The use of this ion-sputtering technique, combined with AES analysis, is very effective in studying the surface chemistry. First, it is possible that two different surface chemistries may be obtained before and after sputtering. Thus, the evidence of some differences in the chemistry between the grain boundary and the matrix may be obtained. Second, by comparing the peak-to-peak amplitude of definite elements by sputtering layer by layer, a depth profile of certain elements from the grain boundary to the inside grain, e.g. matrix, can be easily obtained. This is possible because the AES analysis has a high depth resolution on the order of one monolayer. Examination of this depth profile can tell how the concentration changes with respect to depth.

Many research investigations [41-44] have reported that segregation of impurities, such as S, P, As, Sn, Sb and Bi, to the grain boundary often causes intergranular fracture. In this investigation, however, there are no impurity elements segregated to the grain boundary. There-

fore, the intergranular fracture cannot be explained by impurity segregation to the grain boundary.

Suto and Murakami [49] found that manganese segregates to the grain boundary in 12Ni-6Mn-P alloy during tempering at 375°. Lee [50] indicated that manganese segregates to the grain boundary in Fe-12Mn alloys during tempering at 450°C. In this work, the results of AES analysis indicate that manganese segregates to the grain boundary in the high manganese austenitic Fe-Mn alloy after solution treatment at 1000°C. The magnitude of manganese segregation to the grain boundary is increased with the increasing manganese content in Fe-Mn alloys as shown in Fig. 20. Also, increasing the manganese content of Fe-Mn alloys increases the thickness of the manganese segregation zone. There are two kinds of segregation, e.g. equilibrium segregation and non-segregation. Equilibrium segregation occurs at interfaces such as grain boundaries and surfaces. It is caused by impurity atoms moving to interfaces and, as a result, its free energies are reduced. Usually atoms with large free energies of segregation, e.g. the reduction in energy of segregating atoms in the segregated site, have large differences in size and electronic structure compared with the matrix atoms [51]. The mechanism of non-equilibrium segregation relies on the formation of sufficient quantities of vacancy-solute complexes [52-54]. When material is cooled through a large temperature range, the equilibrium concentration of vacancies, and thus complexes, are reduced. This true equilibrium concentration cannot be realized during fast cooling conditions except at vacancy sinks. Such concentration gradients are formed in quickly-cooled material and there is a net flow of vacancies towards the vacancy

sinks. The vacancy-solute complexes are also carried down these gradients and solute atoms are thus deposited at the sink. Solute segregation then accumulates near the relevant interfaces. Non-equilibrium segregation is dependent on the binding energy of the solute atom to a vacancy. Due to different mechanisms of these two kinds of segregation, the thickness of segregation and the influences of austenitizing temperature and cooling rate on the segregation are different [54-56] (see appendix for further details). Based on these differences, it is possible to distinguish these two kinds of segregation.

A distinguishing feature of equilibrium segregation is that it be localized to within one or two atom distances of the plane of the interface, e.g., 5-10 Å [55,57]. In contrast to equilibrium segregation, the segregation zone of non-equilibrium segregation may range from 1 nm to 1 μm [54,55]. From Fig. 23 the thicknesses of the manganese segregation zone are 37Å, 50Å and 65Å for 35 Mn, 40Mn and 45 Mn alloys, respectively. They are much greater than the thickness of the equilibrium segregation zone.

From Figs. 31 and 32, it can be seen that the manganese segregation increases with the increasing austenitizing temperature. Also, it can be seen from Figs. 35 and 36 that manganese segregation is decreased with decreasing cooling rate. In the case of non-equilibrium segregation, increasing austenitizing temperature increases segregation and decreasing cooling rate decreases segregation. Therefore, based on the results of the thickness of manganese segregation and the influences of austenitizing temperature and cooling rate on the manganese segregation, it can be concluded that the manganese segregation in austenitic Fe-Mn

alloys belong to the non-equilibrium segregation, as boron in 316 austenitic stainless steel [58] and chromium in Cr-Mo steel [59].

As shown in Figs. 5, 20 and 23, increasing the manganese content in Fe-Mn alloys increases the ductile-to-brittle transition temperatures in the Charpy impact test, the extent of intergranular fracture, and the magnitude and extent of manganese grain boundary segregation. Figures 24 and 25 show the relationship between the impact toughness and the manganese segregation.

Increasing austenitizing temperature decreases the impact toughness and increases the manganese grain boundary segregation as shown in Fig. 30 and 33. Also, it can be seen from Figs. 17 and 33 to 36 that decreasing the cooling rate decreases the intergranular fracture, the magnitude and the extent of manganese grain boundary segregation. From these results, it is obvious that the intergranular fracture and embrittlement of high manganese austenitic Fe-Mn alloys at low temperature are caused by manganese segregation to the grain boundaries.

The possible mechanism for intergranular fracture of high manganese austenitic Fe-Mn alloys caused by manganese segregation to the grain boundaries is as follows:

(a) The manganese segregation zone at the grain boundaries is harder than the interior of the grain during the plastic deforming process because manganese decreases the stacking fault energy and increases the strain hardening exponent. The manganese segregation zone acts as a "hard shell" around the grain. The grain boundary itself will cause some degree of dislocation pinning but yielding will eventually occur in the next grain. If the "hard shell" exists at the grain

boundaries, the pileup can be much longer. The stress caused by long pileup can then initiate an intergranular crack at the grain boundaries. Lowering the temperature increases the strain hardening exponent [61], therefore, it increases the tendency to intergranular fracture.

(b) Breedis [26] has shown that the tendency for faulting in fcc steels increases as the temperature of deformation decreases. The stacking faults are more easily formed in the manganese segregation zone during deformation. The high local shear associated with the faults could cause the fracture strain to be exceeded in the vicinity of the faults. The resultant crack could possible propagate catastrophically under the existing state of stress before the energy of deformation could be absorbed by other parts of a specimen [25].

(c) Due to the manganese segregation to the grain boundary and the non-uniform deformation between the manganese segregation zone and the interior of the grain, local internal stresses are accumulated. The local internal stress will promote the intergranular fracture [27,49,60].

The determination that the manganese segregation to the grain boundaries is the source of intergranular fracture is of great importance. This knowledge will help to develop high performance high manganese austenitic cryogenic steels by optimizing the chemical composition and making a suitable heat treatment procedure for these steels. Adding some other alloying elements that also segregate to the grain boundaries, such as B [58] and Cr [59], may reduce manganese segregation to the grain boundaries. An implication of the fracture mechanism described above is that the toughness of high manganese steels can be

improved as the stacking fault energy of these steels increases. Dulien and Nutting [34] have shown that nickel and chromium raise the stacking fault energy. Aluminum also has high stacking fault energy [32]. Therefore, adding Cr, Ni and Al will increase the low temperature toughness of high manganese austenitic steels and many high performance Cr-Mn-Ni-N and Fe-Al-Mn high manganese austenitic cryogenic steels are developed. In order to minimize the manganese segregation and improve the low temperature toughness, the heat treatment process of high manganese austenitic steel should keep the solid-solution temperature and the following cooling rate as low as possible.

V. CONCLUSIONS

(1) The high manganese austentitic Fe-Mn alloys used in this research work are very stable at 77 K. Even after deformation at 77 K, only approximately 2% ε was found in the 35% Mn alloy and no ε was found in the 40 and 45% Mn alloys. These Fe-Mn alloys exhibit a ductile-to-brittle transition phenomenon in impact test. The toughness transition is accompanied by a change of fracture mechanism from microvoid coalescence to intergraular fracture. The transition temperature is increased with increasing manganese content.

(2) The yield strength and ultimate tensile strength of different Fe-Mn alloys are almost the same. The strain hardening exponent, uniform plastic deformation, total plastic deformation, and true stress at maximum load all are increased with increasing manganese content.

(3) The segregation of certain impurities, such as P, S, Sn, As, Sb and Bi, to grain boundaries is one of the major causes of intergranular fracture. No segregation of impurity elements to grain boundaries was found in this research work.

(4) In this investigation, the results of AES analyses indicate that manganese segregates to the grain boundaries in the high manganese austenitic Fe-Mn alloy after solution treating at 1000°C. The magnitude and extent of manganese segregation to grain boundaries are increased with increasing manganese content. The manganese segregation is a kind of non-equilibrium segregation. Increasing the solid-solution treatment temperature and the following cooling rate increases the manganese segregation to the grain boundaries.

(5) The ductile-to-brittle transition temperature, the extent of intergranular fracture, and the magnitude and extent of manganese segregation to the grain boundaries are increased with increasing the manganese content of Fe-Mn alloys, solid-solution treatment temperature, and the subsequent cooling rate. It appears that intergranular fracture and embrittlement of high manganese austenitic Fe-Mn alloys at low temperature are caused by manganese segregation to the grain boundaries. The possible mechanism for intergranular fracture of high manganese austenitic Fe-Mn alloys caused by manganese segregation is discussed.

(6) The finding that the manganese segregation to the grain boundaries is the source of intergranular fracture is of great importance. This knowledge will help in the development of high performance, high manganese, austenitic cryogenic steels and other high manganese steel by optimizing the chemical composition of the steel and developing a suitable heat treatment procedure.

APPENDIX

The Differences between Equilibrium Segregation and Non-equilibrium Segregation

Equilibrium Segregation	Non-equilibrium Segregation
(1) Mechanism	
Equilibrium segregation occurs at the interface such as grain boundaries and surfaces. It is caused by impurity atoms (S,P,As,Sn,Sb,Pb and Bi) moving to interfaces and, reduced. Usually atoms with large free energies of segregation, e.g. the reduction in energy of segregating atom in the segregated site, have large differences in size and electronic structure compared with the matrix atom [51].	When material is cooled through a large temperature range the equilibrium concentration of vacancies and thus vacancy-solute complexes is reduced. Therefore vacancies flow to the interfaces where they may be readily annihilated. The vacancy-solute complexes are also carried down these gradients and solute atoms are thus deposited at the sink. Solute segregation then accumulates near the relevant interface. Non-equilibrium segregation is dependent upon the binding energy of the solute atom to a vacancy [52-54].

(2) Effect of Temperature

$$\frac{C_b}{C_g} = A \exp\left(\frac{E}{K T}\right)$$

C_b: segregating atom concentration on the boundary

C_g: segregating atom concentration in the unsegregated regions

K: Boltzman's constant

E: free energy of segregation

This equation shows that equilibrium segregation is greater at low temperatures [54].

$$C_c = K_c K_v C_x \exp\frac{(E_b - E_f)}{T}$$

C_c: concentration of complex

C_s: concentration of solute

E_b: vacancy solute binding energy

Since E_b will rarely exceed E_f increasing the temperature will therefore increase the concentration of complex and segregation [54-56].

(3) Effect of Time and Cooling Rate

At any given temperature, there is a unique solute concentration for each of these sites that is asymptotically approached as times go to infinity and at a rate governed by diffusion.

Non-equilibrium segregation depends on rate processes and kinetic events and, in general, it disappears as time approaches infinity if diffusion processes are allowed to reach full equilibrium.

Decreasing cooling rate will increase segregation [50-56].

Decreasing cooling rate will decrease segregation [54-56].

(4) Thickness of Segregation Zone

It has now been experimentally confirmed that the space occupied by the segregation is constrained to within the structurally perturbed region of the interface. Hence, a distinguishing feature of equilibrium segregation is that it will be localized to within one or two atom distances of the plane of the interface [54,55,60].

In contrast to equilibrium segregation, various phenomena exist in which the apparent levels of segregation build-up may extend to distances of as much as several μm (10^4 Å) across grain boundaries [54,55,64].

REFERENCES

1. A. Holden, J.D. Bolton and E.R. Petty: J. Iron and Steel Inst., 209, Sept. (1971) p. 721.
2. C.E. Spaeder, Jr., et al.: Metal Eng. Quart. 9:3 (1969) p. 1.
3. Tetsuo Kato, Shoichi Fukui, Masakuni Fujikura and Kiyohito Ishida: Trans. I.S.I.J., 16 (1976) p. 673.
4. Keisuke Ishikawa, et al.: Iron and Steel (Japan) 65 (1979) p. 219.
5. Hirofumi Yoshimura, et al.: Trans. I.S.I.J. 20 (1980) p. 187.
6. T. Horiuchi, R. Ogawa, M. Shimada, S. Tone, M. Yamaga and Y. Kasamatsu: Adv. in Cryogenic Eng., vol. 28 (1981) p. 93.
7. J. Charles, A. Lutts and A. Berghezan: Adv. Cryogenic Eng. Mat., vol. 28 (1981) p. 105.
8. H. Yoshimura, H. Masumoto and T. Inoue: Adv. Cryogenic Eng. Mat, vol. 28 (1981) p. 115.
9. K.A. Yushchenko, V.I. Belotzerkovetz, A.G. Kvasnevskii and A.V. Shavel: Adv. Cryogenic Eng. Mat., vol. 28 (1981) p. 833.
10. S. Tone, M. Shimade, T. Horiuchi, Y. Kasamatsu, H. Nakajima and S. Shimamoto: Adv. Cryogenic Eng. Mat., vol. 30 (1983) p. 145.
11. K. Shibata, Y. Kobiki, Y. Kishimoto and T. Fujita: Adv. Cryogenic Eng. Mat., vol. 30 (1983) p. 153.
12. C.H. Shi, Y.S. Zhang, Y.K. Xu and Y.Y. Li: Adv. Cryogenic Eng. Mat., vol. 30 (1983) p. 161.
13. H. Masumoto and K. Suemune: Adv. Cryogenic Eng. Mat., vol. 30 (1983) p. 169.
14. R. Ogawa and J.W. Morris, Jr.: Adv. Cryogenic Eng. Mat., vol. 30 (1983) p. 177.

15. H. Nakajima, K. Yoshida, Y. Takahasi, E. Tada, M. Oshikiri, K. Koizumi, S. Shimamoto, R. Miura, M. Shimada, S. Tone, H. Masumoto and T. Sakamoto: Adv. Cryogenic Eng. Mat., vol. 30 (1983) p. 219.

16. R. Miura, H. Nakajima, Y. Takahasi and K. Yoshida: Adv. Cryogenic Eng. Mat., vol. 30 (1983) p. 245.

17. F.W. Schaller and V.F. Zackey: Trans. ASM, 51 (1959) p. 609.

18. A. Kasak and E.J. Dulis: Trans. ASM 51 (1959) p. 623.

19. J.C. Shyne, F.W. Schaller and V.F. Zackey: Trans. ASM 52 (1960) p. 848.

20. G.F. Tisniai and C.H. Samans: Trans. ASM 52 (1959) p. 623.

21. J. Mukherjee and B.R. Nijahau: J. Iron and Steel Inst., 204 (1967) p. 62.

22. M.M. Belenkova, I.I. Kodlubik, K.A. Malyshev, M.N. Mikheyel, V.D. Sadovskii and P.A. Ustyvgov: Phys. Met. Metallography, 10 (1960) p. 111.

23. V.I. Grigorkin: Metal Sci. and Heat Treatment, July (1969) p. 568.

24. J. Thomson: Trans. ASM, 52 (1960) p. 853.

25. J.D. Defilippi, K.G. Brickner and E.M. Gilbert: Trans. of Metall. Soc., AIME, 245 (1969) p. 2141.

26. J.F. Breedis: Acta Metall., 13 (1965) p. 239.

27. Hajime Suto and Byon Sun Chun: Tech. Report, 44, Tohoku University, (1979) p. 317.

28. A.P. Gulyaev and V.M. Chulkova: Metal Sci. and Heat Treatment, 16 (1974) p. 332.

29. A.P. Gulyaev and T.F. Volynova: Metal Sci. and Heat Treatment, (2979) p. 98.

30. Jirou Namekata and Yoshihiro Kondo: Presented at the 104th I.S.I.J. Meeting, October, 1982.

31. Mark Jay Schonfein: Lawrence Berkeley Laboratory Report 2749, August, 1974.

32. Richard W. Hertzberg: "Deformation and Fracture Mechanics of Engineering Materials," John Wiley and Sons, 2nd ed., 1983.

33. I. Tamura: J. Iron and Steel Inst. (Japan) 56 (1979) p. 61.

34. D. Dulieu and J. Nutting: "Metallurgical Development in High-Alloy Steels, ISS Special Report 86 (1964) Iron and Steel Inst., England

35. Y. Tomota and J.W. Morris, Jr. Presented at the 107th ISIJ meeting, April, 1984, Lecture No. S503.

36. L.E. Davis: Modern Surface Analysis, Metallurgical Application of Auger Electron Spectroscopy (AES) and X-ray Photo-electron Spectroscopy (XPS, Las Vegas, Nev., Feb. 23-24, 1980.

37. W.C. Johnson: Ibid, p. 22.

38. A. Joshi: "Interfacial Segregation", W.C. Johnson and J.M. Bladely (eds.) ASM (1977) p. 39.

39. P.W. Plamberg and H.L. Marcus: Trans. ASM 62 (1969) p. 1016.

40. D. Briggs and M.P. Seah: "Practical Surface Analysis", John Wiley and Sons (1983).

41. C.J. McMahon, Jr., V. Vitek and J. Kameda: "Developments in Fracture Mechanics," vol. 2, G.G. Chell (ed.), Applied Science Publishers (1979) p. 193.

42. C.L. Briant and S.K. Banerji: "Treatise on Materials Science and Technology," vol. 25, Academic Press (1983) p. 21.

43. H.L. Marcu, L.H. Hackett, Jr. and P.W. Palmberg: "Temper Embrittlement of Alloy Steels," ASTM STP 499 (1972) p. 90.

44. B.J. Schulz and C.J. McMahon, Jr.: "Temper Embrittlement of Alloy Steels," ASTM STP 499 (1972) p. 104.

45. A.H. Cottrell: "Dislocation and Plastic Flow in Crystals", Claredon Press, Oxford, England (1953).

46. C.L. Briant and S.K. Banerji: Int. Metals Rev. No. 4 (1978) Rev. 232.

47. J.R. Lon, Jr.: Prog. Material. Sci., (1963) 12.1.

48. J.M. Berry: Trans. ASM 51 (1959) p. 556.

49. Hajine Suto and Taku Murakami: Trans. J.I.M. 20 (1979) p. 365.

50. Hyung Jai Lee: Lawrence Berkeley Laboratory Report 14747, June, 1982.

51. E.D. Hondros and D. McLean: Surface Phenomena of Metals, 28 (1968) p. 39.

52. K.T. Aust, S.J. Armijo, E.F. Koch and J.A. Westbrook: Trans. ASM, 60 (1967) p. 360.

53. T.R. Anthony: Acta Metall., 17 (1969) p. 603.

54. R.G. Faulkner: J. Materials Sci., 16 91981) p. 373.

55. E.D. Hondros and M.P. Seah: "Physical Metallurgy," (3rd Ed.), R.W. Cahn and P. Hassen (eds.), North Holland Physics Pub. (1983) p. 856.

56. R.G. Faulkner: "Advances in the Physical Metallurgy and Applications of Steels," The Metals Society, London (1982) p. 266.

57. D.Y. Lee, E.V. Arrera, J.P. Stark and H.L. Marcus: Met. Trans. 15A (1984) p. 1415.

58. T.M. Williams, A.M. Stoneham and D.R. Harries: Metal Sci., 10 (1976) p. 14.

59. P. Doig and P.E.J. Flewitt: Acta Metall., 29 (1981) p. 1831.

60. A.S. Drachinsky: Phys. Met. Metallography, 55 (1983) p. 164.

61. Y.G. Kim, Y.S. Park and J.K. Han: Met. Trans 16A (1985) p. 1689.

Table 1. Chemical Composition of Fe-Mn Alloy in weight percent.

Alloy	C	Mn	N	O	P	S
35Mn	<0.001	34.46	0.007	0.018	0.010	0.008
40Mn	<0.001	40.04	0.015	0.022	0.009	0.011
45Mn	<0.001	45.23	0.018	0.023	0.014	0.012

Table 2. Tensile Properties of Fe-Mn Alloys.

Alloy	Y.S. MPa (ksi)	U.T.S. MPa (ksi)	Elongation %	R.A. %	T.S.[1] MPa (ksi)	U.R.A.[2] %	n[3]
35Mn	294.0 (42.6)	750.0 (108.6)	05.5	71.0	1125.0 (163.0)	33.0	0.41
40Mn	299.0 (43.3)	785.0 (113.6)	60.0	64.0	1221.0 (176.8)	36.0	0.45
45Mn	294.0 (42.6)	760.0 (110.0)	81.0	75.0	1368.0 (198.1)	44.0	0.58

[1] True stress at maximum load.
[2] Uniform reduction of area at maximum load.
[3] Strain hardening exponent, $\sigma = K \cdot \varepsilon^n$

Table 3. Microstructure Determined by X-Ray Diffraction.

Alloy	Microstructure	
	After cooled to 77 K	After deformation at 77 K
35Mn	γ	~ 2% ε + γ
40Mn	γ	γ
45Mn	γ	γ

FIGURE CAPTIONS

1. Standard Charpy impact test specimen.
2. Round tensile specimen.
3. Single notched AES specimen for fracturing.
4. Schematic diagram of the ultra high vacuum reaction chamber with *in-situ* fracturing and cooling stage for AES study.
5. Ductile-brittle transition curves of austenitic Fe-Mn alloys.
6. Tensile test curve of 35 Mn alloy.
7. Tensile test curve of 45Mn alloy.
8. Tensile test curve of 45Mn alloy unloaded at maximum load.
9. SEM fractographs of 35Mn impact specimen broken at $-102^{\circ}C$.
10. SEM fractographs of 35Mn impact specimen broken at $-196^{\circ}C$.
11. SEM fractographs of 40Mn impact specimen broken at $-102^{\circ}C$.
12. SEM fractographs of 40Mn impact specimen broken at $-196^{\circ}C$.
13. SEM fractographs of 45Mn impact specimen broken at $-102^{\circ}C$.
14. SEM fractographs of 45Mn impact specimen broken at $-196^{\circ}C$.
15. AES spectra obtained from intergranular fracture surface and sputtered surface of 35Mn (a) and its SEM fractograph (b).
16. AES spectra obtained from intergranular fracture surface and sputtered surface of 40Mn (a) and its SEM fractograph (b).
17. AES spectra obtained from intergranular fracture surface and sputtered surface of 45Mn (a) and its SEM fractograph (b).
18. Manganese concentration at grain boundaries and grain interior of Fe-Mn alloys.

19. The relationship of manganese content between grain boundaries and grain interior.
20. The increment of manganese content at grain boundaries as a function of manganese content of Fe-Mn alloys.
21. Depth profiles obtained from the intergranular fracture surface of 35Mn.
22. Depth profiles obtained from the intergranular fracture surface of 40Mn.
23. The thickness of manganese segregation zone as a function of manganese content of Fe-Mn alloys.
24. The relationship between the -196°C Charpy impact value and the magnitude of manganese segregation.
25. The relationship between the -196°C Charpy impact value and the extent of manganese segregation.
26. The heat treatment processes for studying the effect of austenitizing temperature.
27. The relationship between the -196°C Charpy inpact value and the austenitizing temperature.
28. AES spectra obtained from intergranular fracture surface and sputtered surface of 45Mn austenitized at 1150°C (a) and its SEM fractograph (b).
29. AES spectra obtained from intergranular fracture surface and sputtered surface of 45Mn austenitized at 1150°C and 1000°C (a) and its SEM fractograph (b).

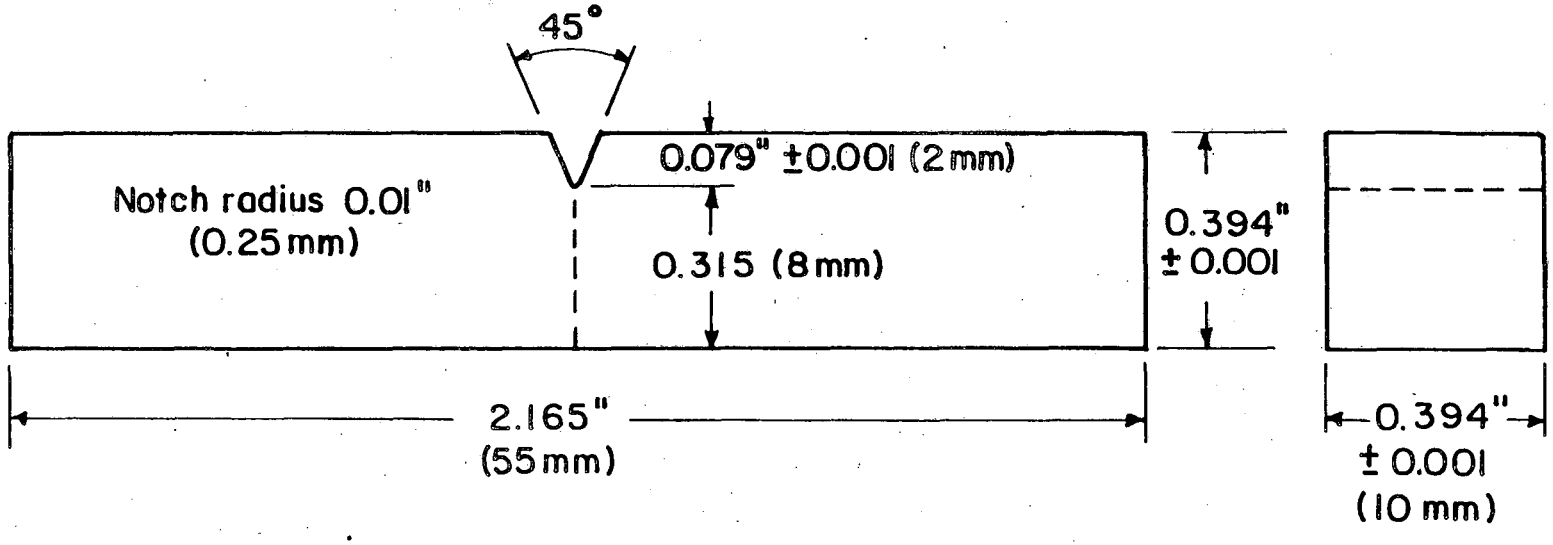

XBL 8110-6792

Figure 1

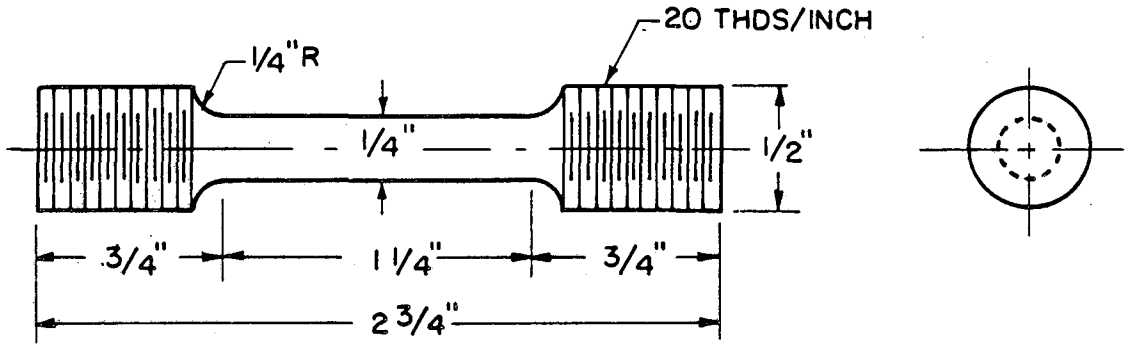

(b) ROUND TENSILE SPECIMEN

XBL735-6189A

Figure 2

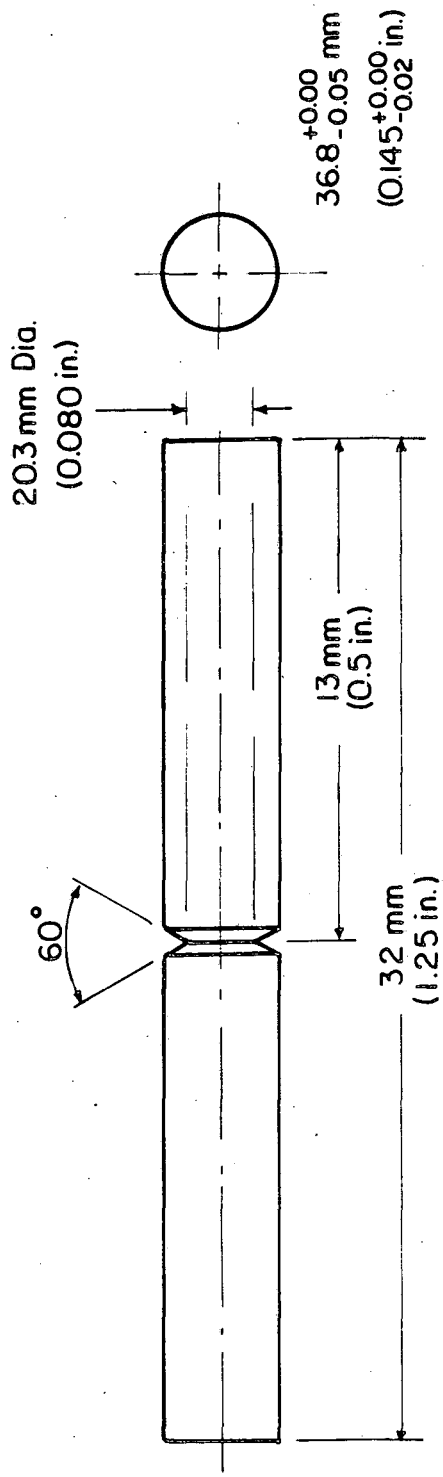

XBL 8510-6736

Figure 3

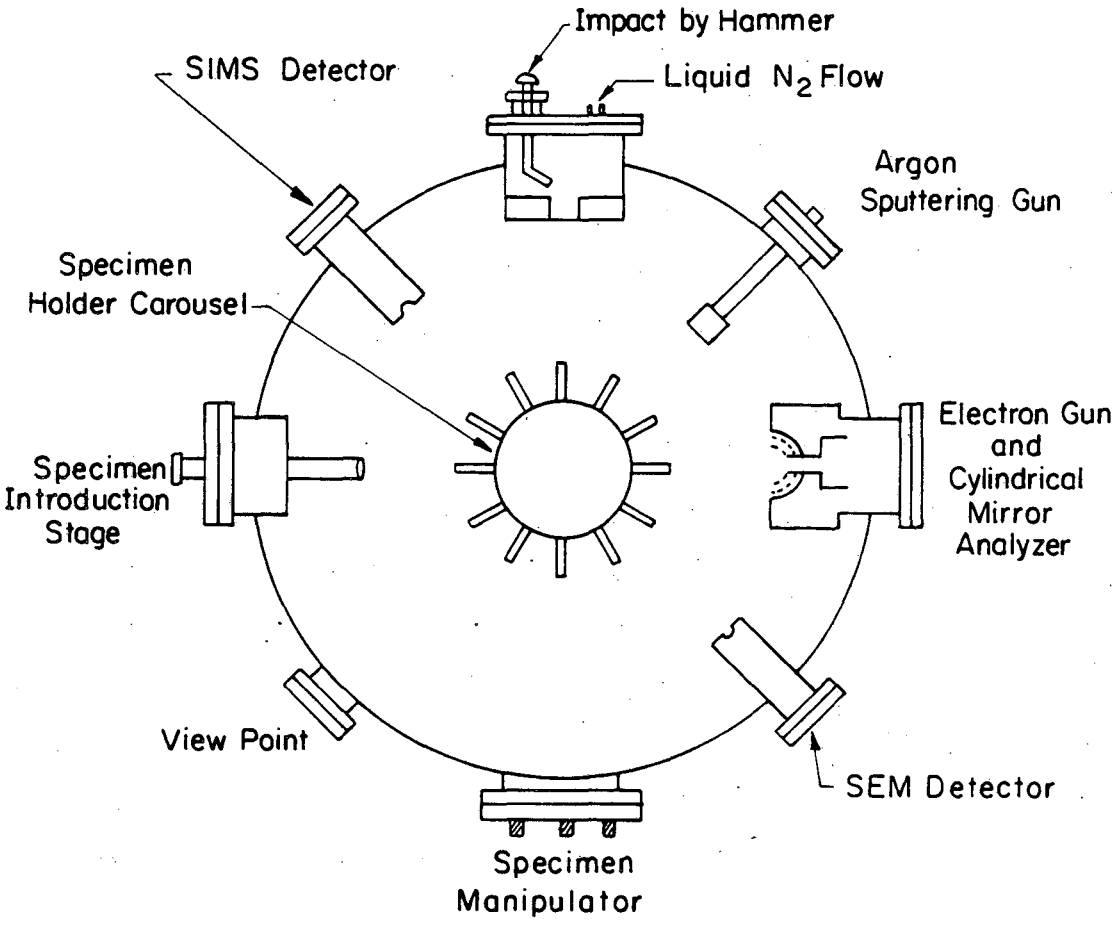
Impact by Hammer
SIMS Detector
Liquid N_2 Flow
Argon
Sputtering Gun
Specimen
Holder Carousel
Specimen
Introduction
Stage
Electron Gun
and
Cylindrical
Mirror
Analyzer
View Point
SEM Detector
Specimen
Manipulator
XBL 812-5241

Figure 4

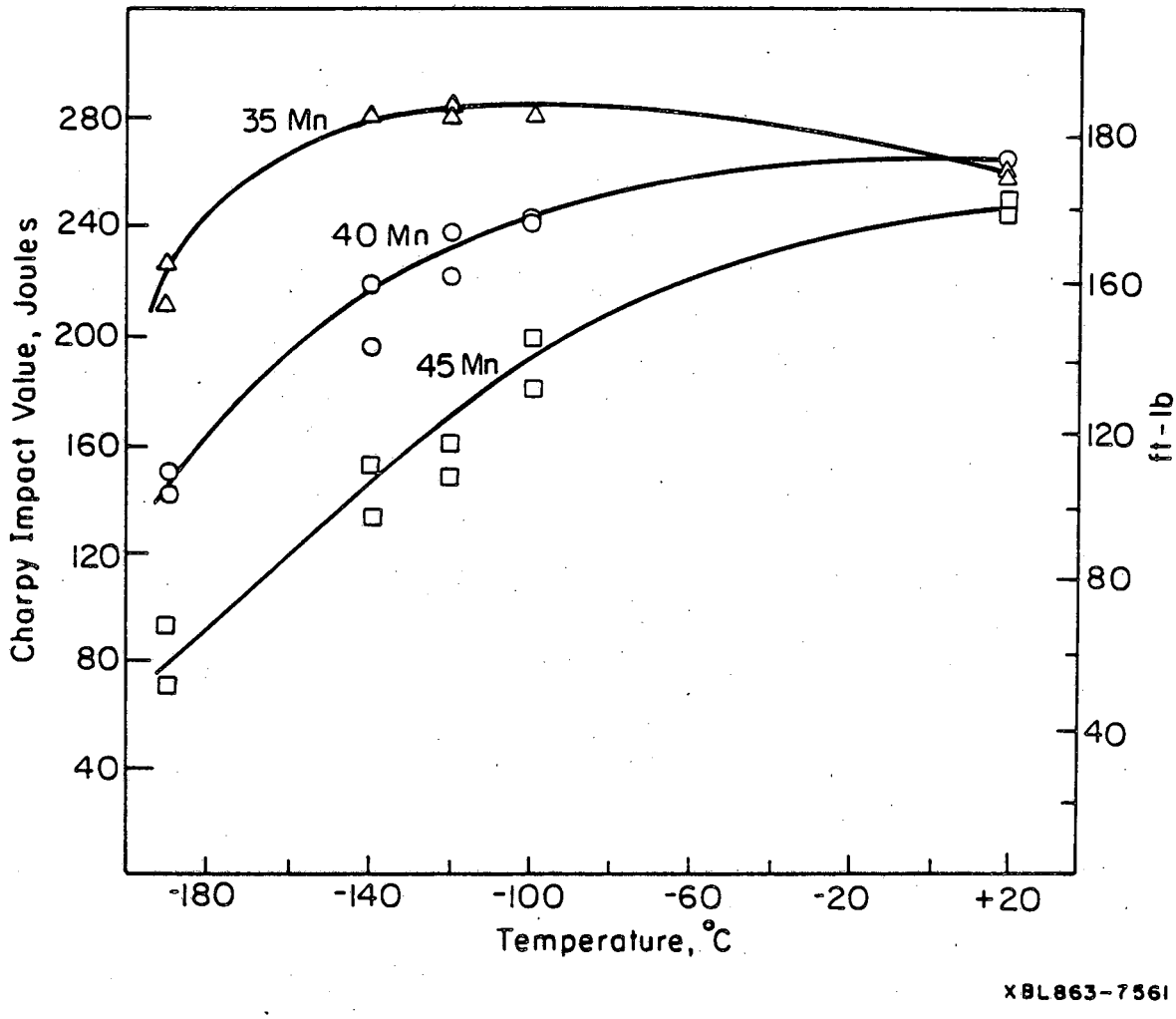
35 Mn
40 Mn
45 Mn
Charpy Impact Value, Joules
ft-lb
Temperature, °C
280
240
200
160
120
80
40
180
160
120
80
40
-180
-140
-100
-60
-20
+20
XBL863-7561

Figure 5

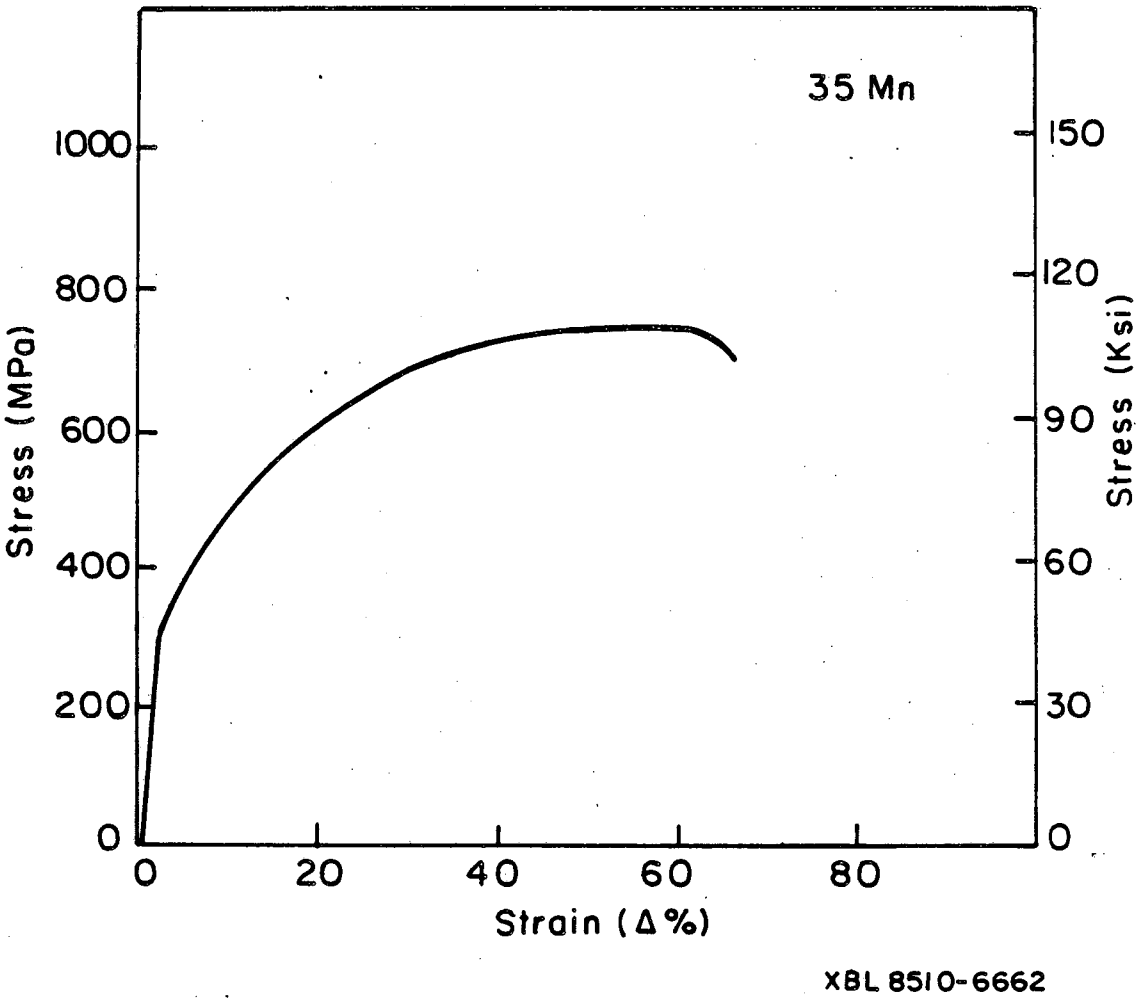
35 Mn
1000
800
600
400
200
0
Stress (MPa)
150
120
90
60
30
0
Stress (Ksi)
0
20
40
60
80
Strain (Δ%)
XBL 8510-6662

Figure 6

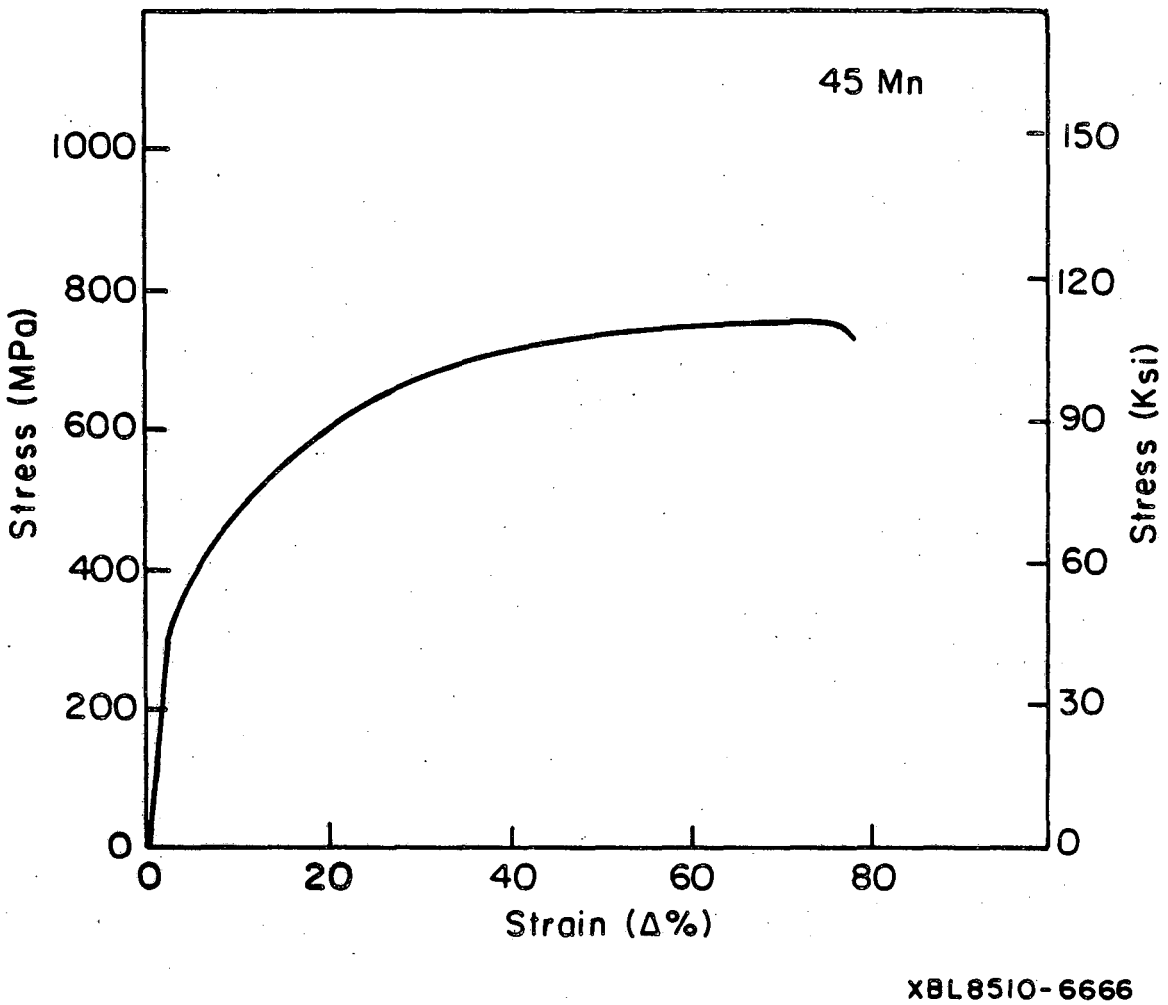
45 Mn
1000
800
600
400
200
0
Stress (MPa)
150
120
90
60
30
0
Stress (Ksi)
0
20
40
60
80
Strain (Δ%)
XBL8510-6666

Figure 7

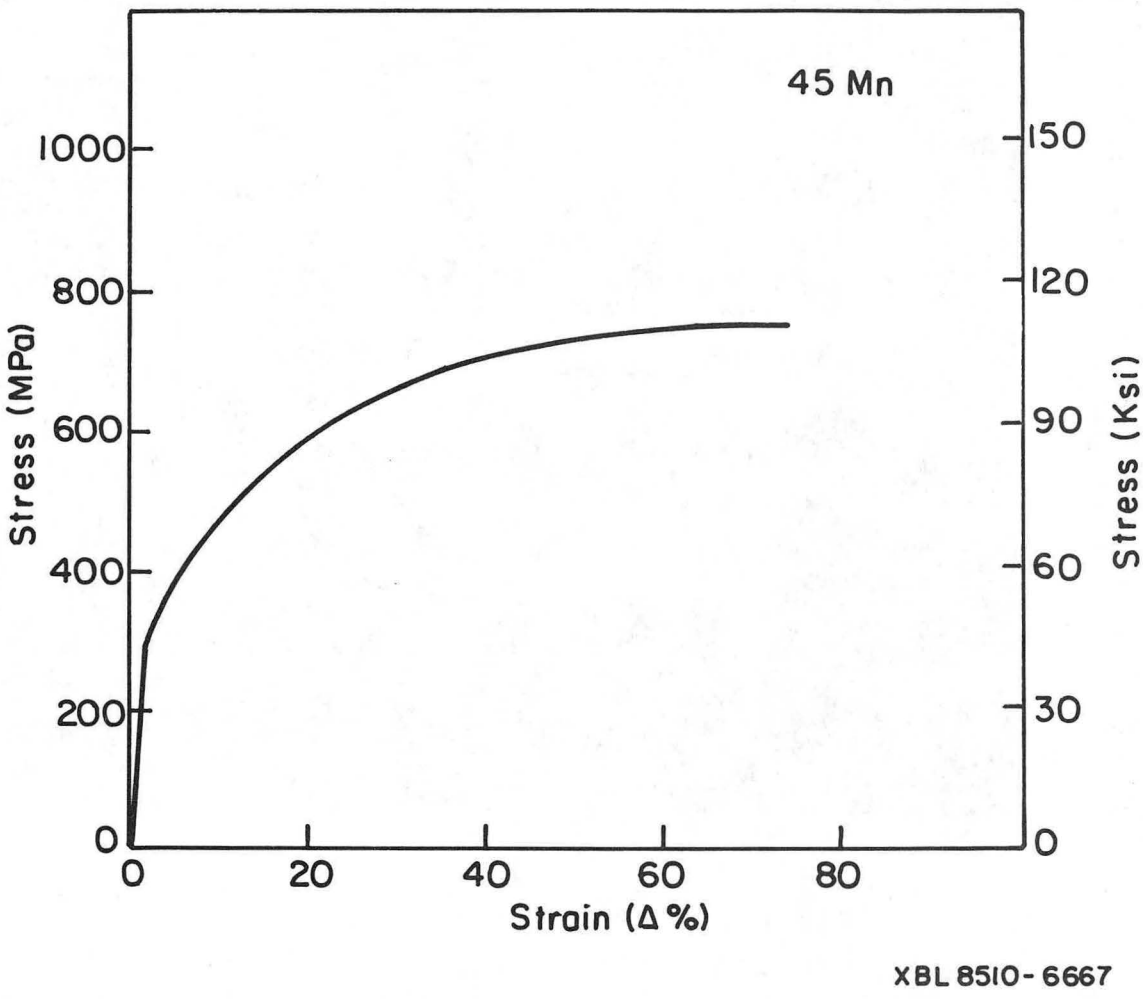
45 Mn
1000
800
600
400
200
0
Stress (MPa)
150
120
90
60
30
0
Stress (Ksi)
0
20
40
60
80
Strain (Δ %)
XBL 8510-6667

Figure 8

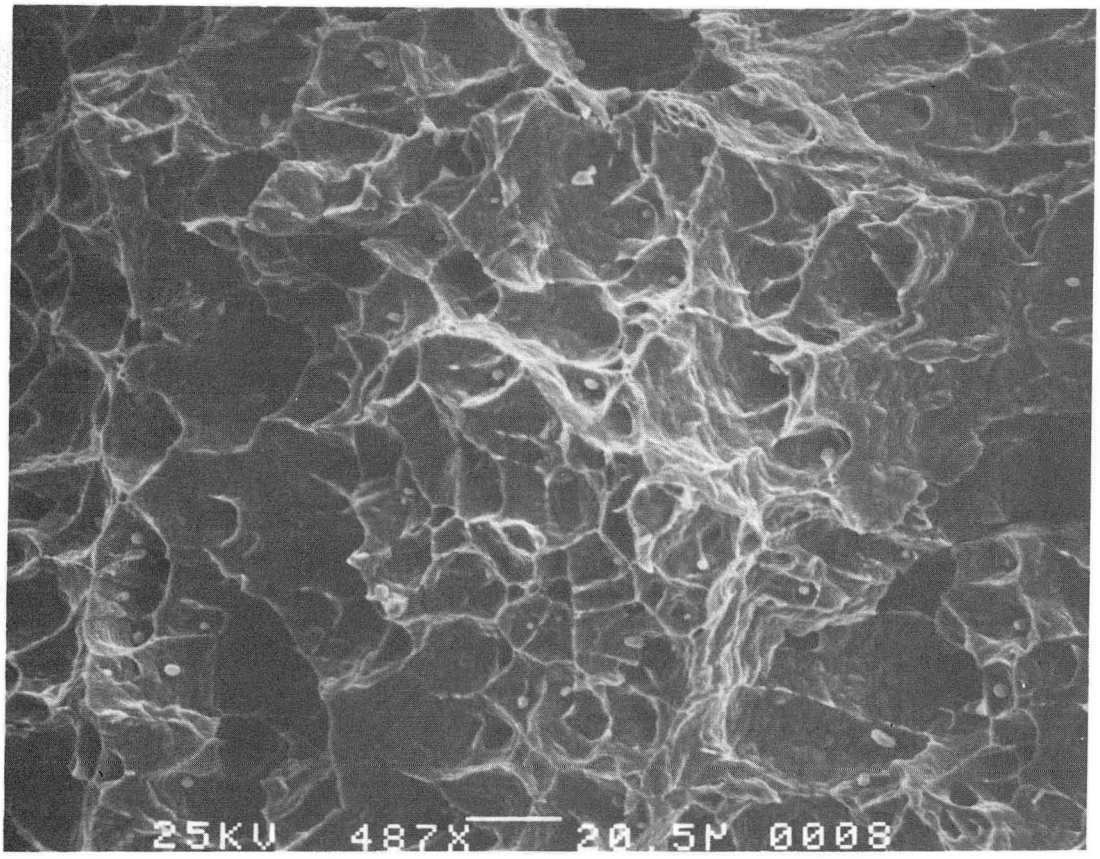

XBB 859-7923

35%Mn-Fe
Solution Treatment: 1000 C, Water Quenching
Impact Testing Temperature: -102 C

Figure 9

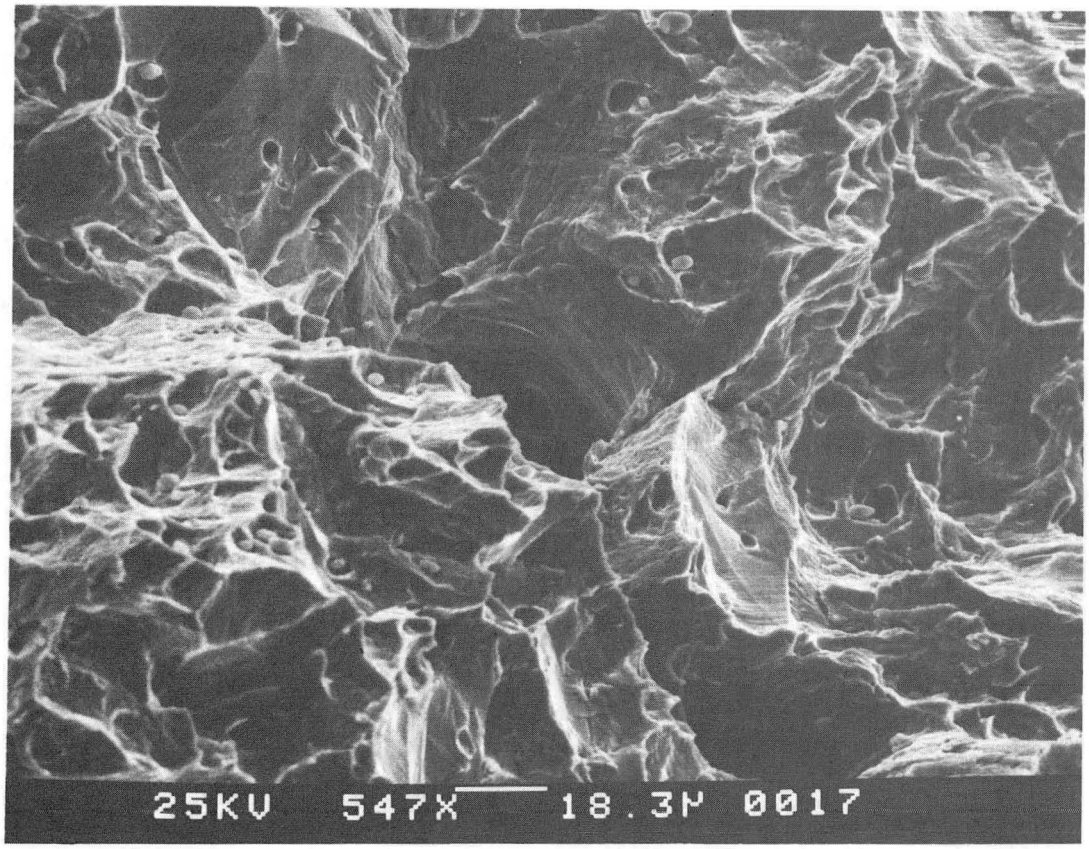

XBB 859-7925

35%Mn -Fe
Solution Treatment: 1000 C, Water Quenching
Impact Testing Temperature: -196 C

Figure 10

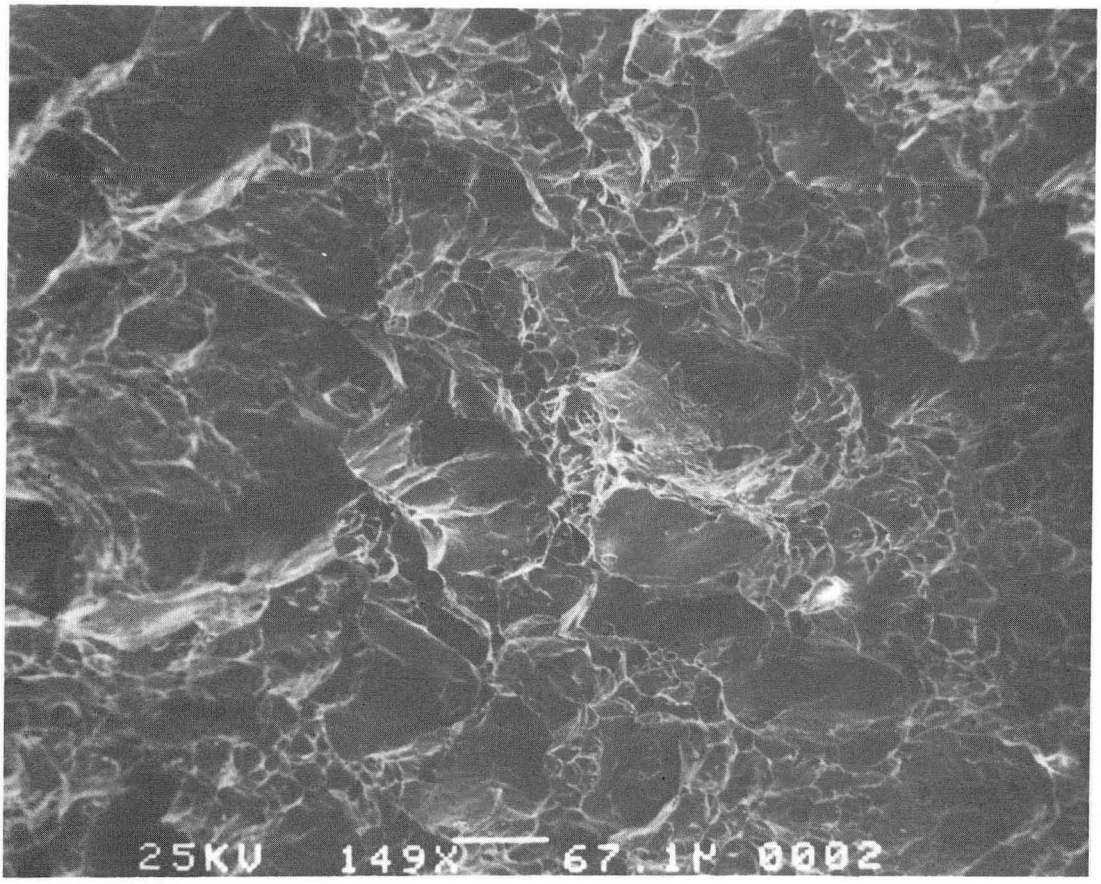

XBB 859-7921

40%Mn-Fe
Solution Treatment: 1000 C, Water Quenching
Impact Testing Temperature: -102 C

Figure 11(a)

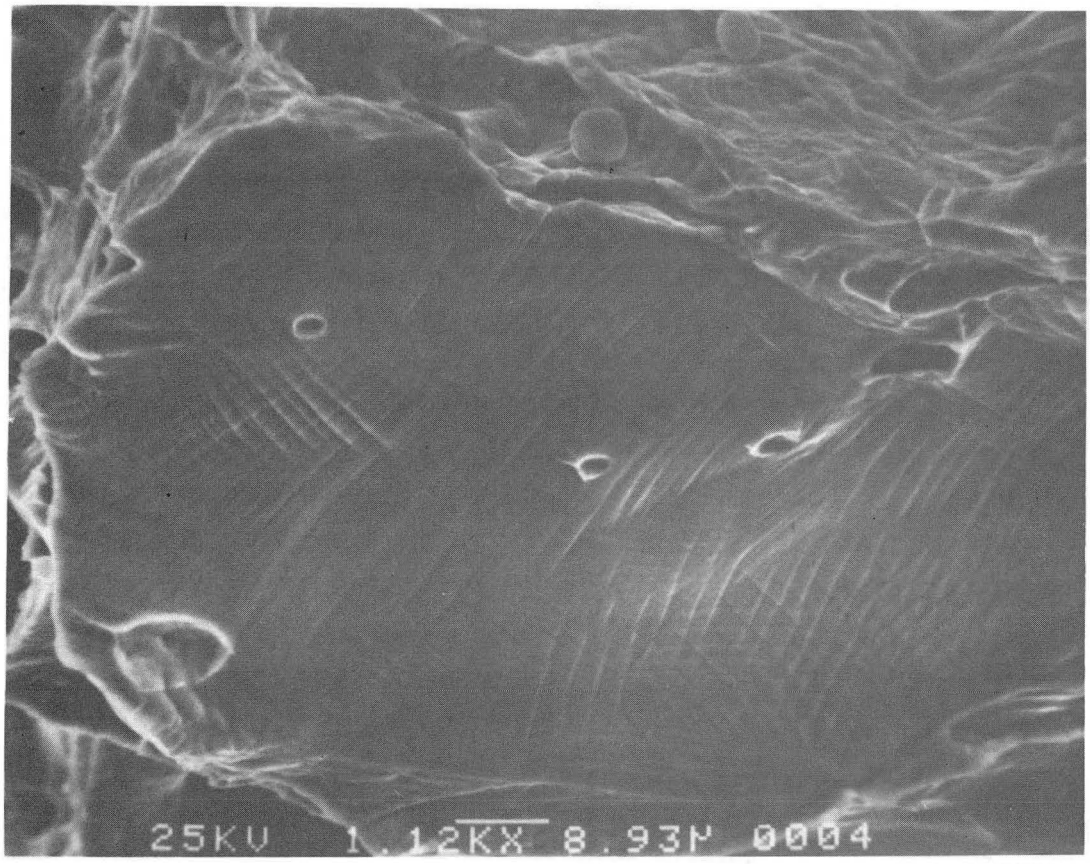

XBB 859-7928

40%Mn-Fe
Solution Treatment: 1000 C, Water Quenching
Impact Testing Temperature: -102 C

Figure 11(b)

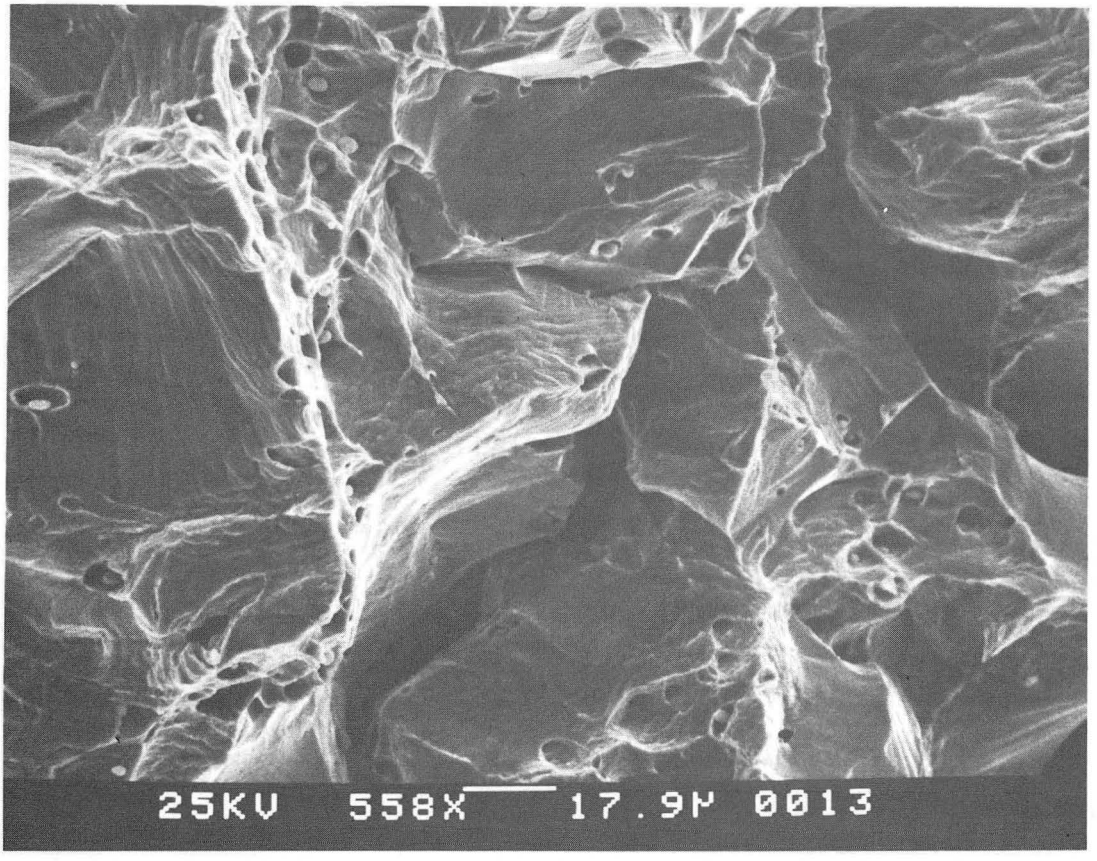

XBB 859-7927

40%Mn-Fe
Solution Treatment: 1000 C, Water Quenching
Impact Testing Temperature: -196 C

Figure 12

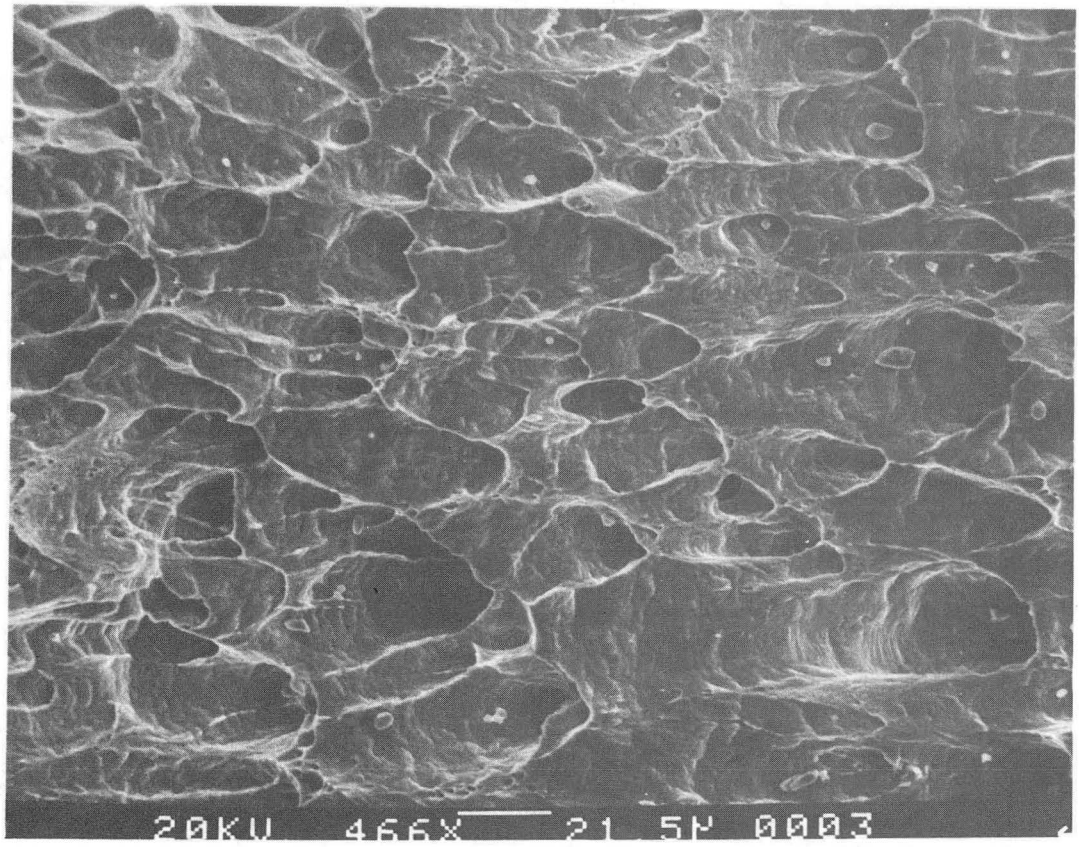

XBB 859-7932

45%Mn-Fe
Solution Treatment: 1000 C, Water Quenching
Impact Testing Temperature: -102 C

Figure 15

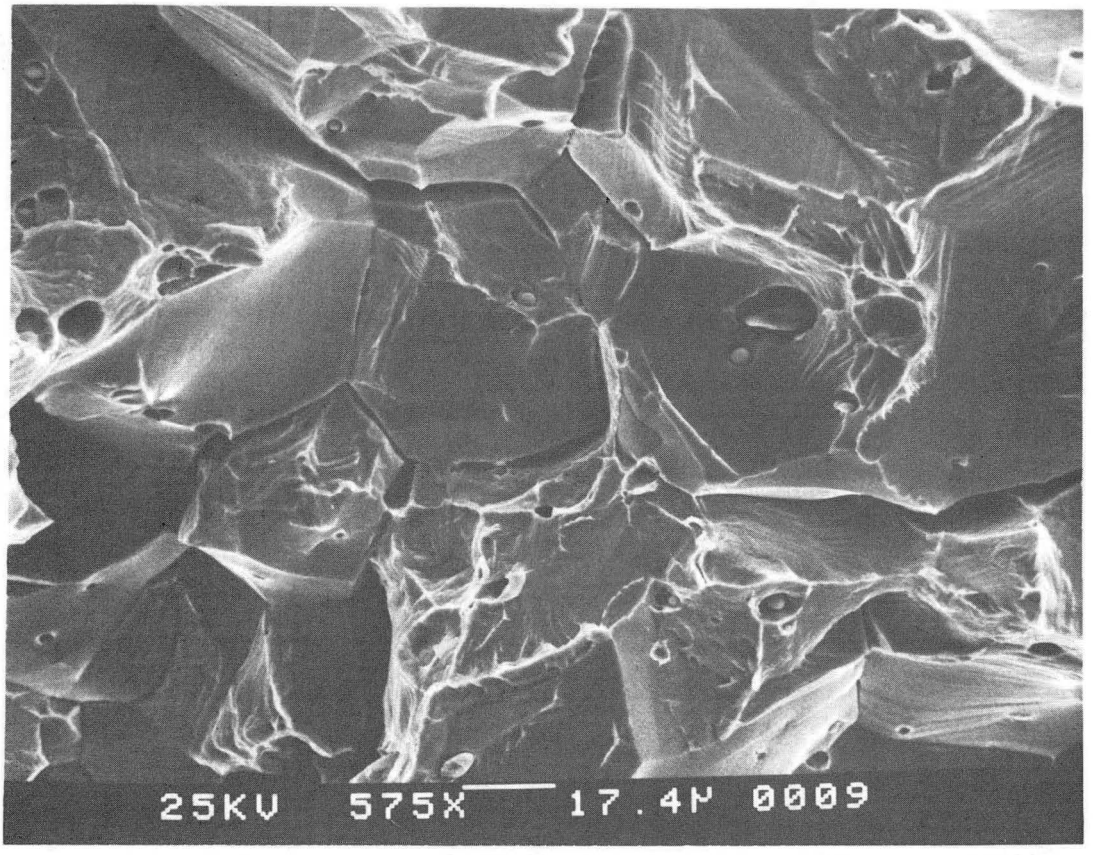

XBB 859-7929

45%Mn-Fe
Solution Treatment: 1000 C, Water Quenching
Impact Testing Temperature: -196 C

Figure 14

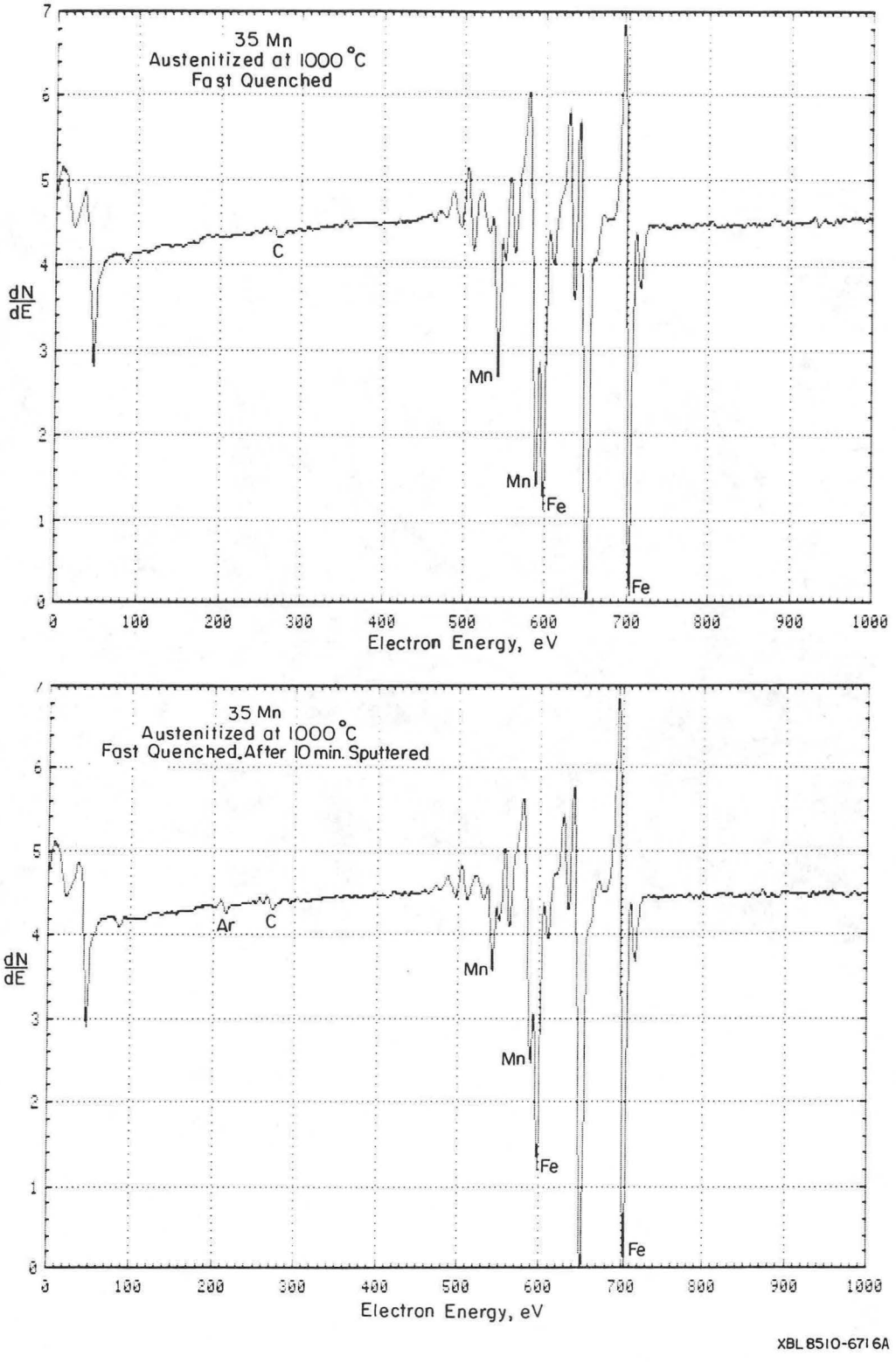
35 Mn
Austenitized at 1000 °C
Fast Quenched
C
Mn
Mn
Fe
Fe
dN/dE
Electron Energy, eV
35 Mn
Austenitized at 1000 °C
Fast Quenched, After 10 min. Sputtered
Ar
C
Mn
Mn
Fe
Fe
dN/dE
Electron Energy, eV
XBL 8510-6716A

Figure 15(a)

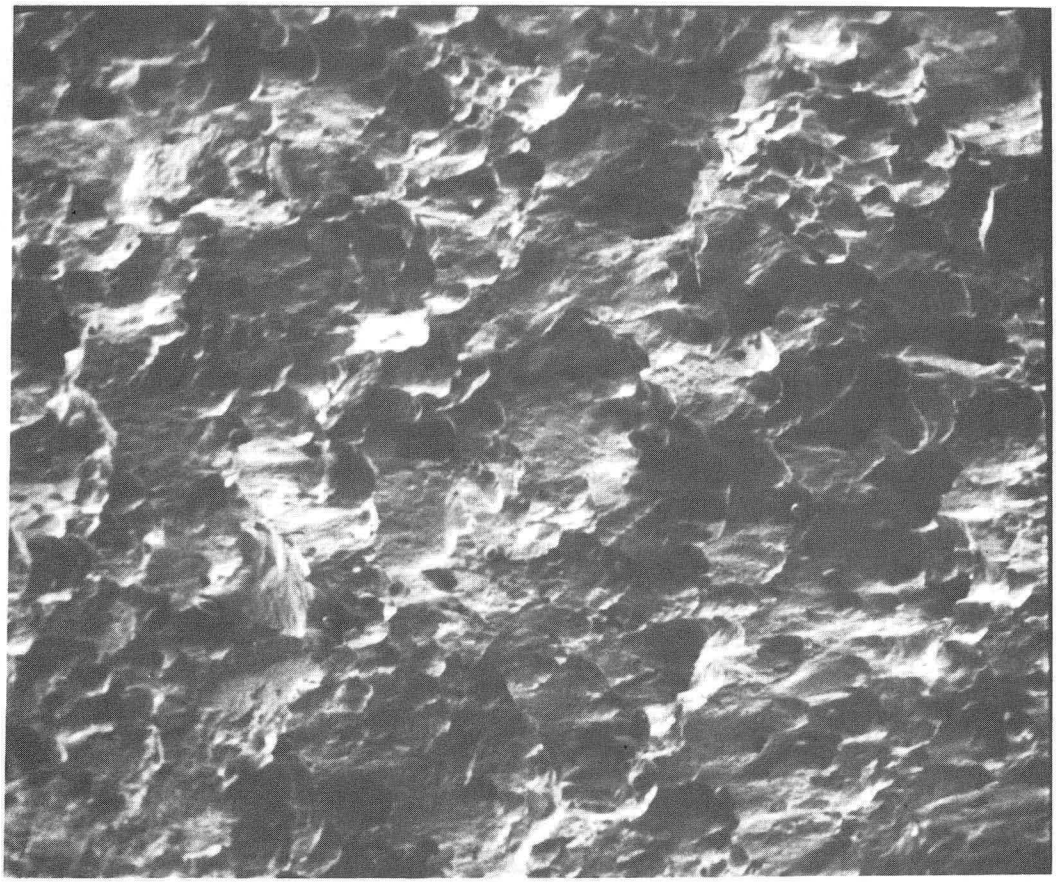

XBB 863-1681

Figure 15(b)

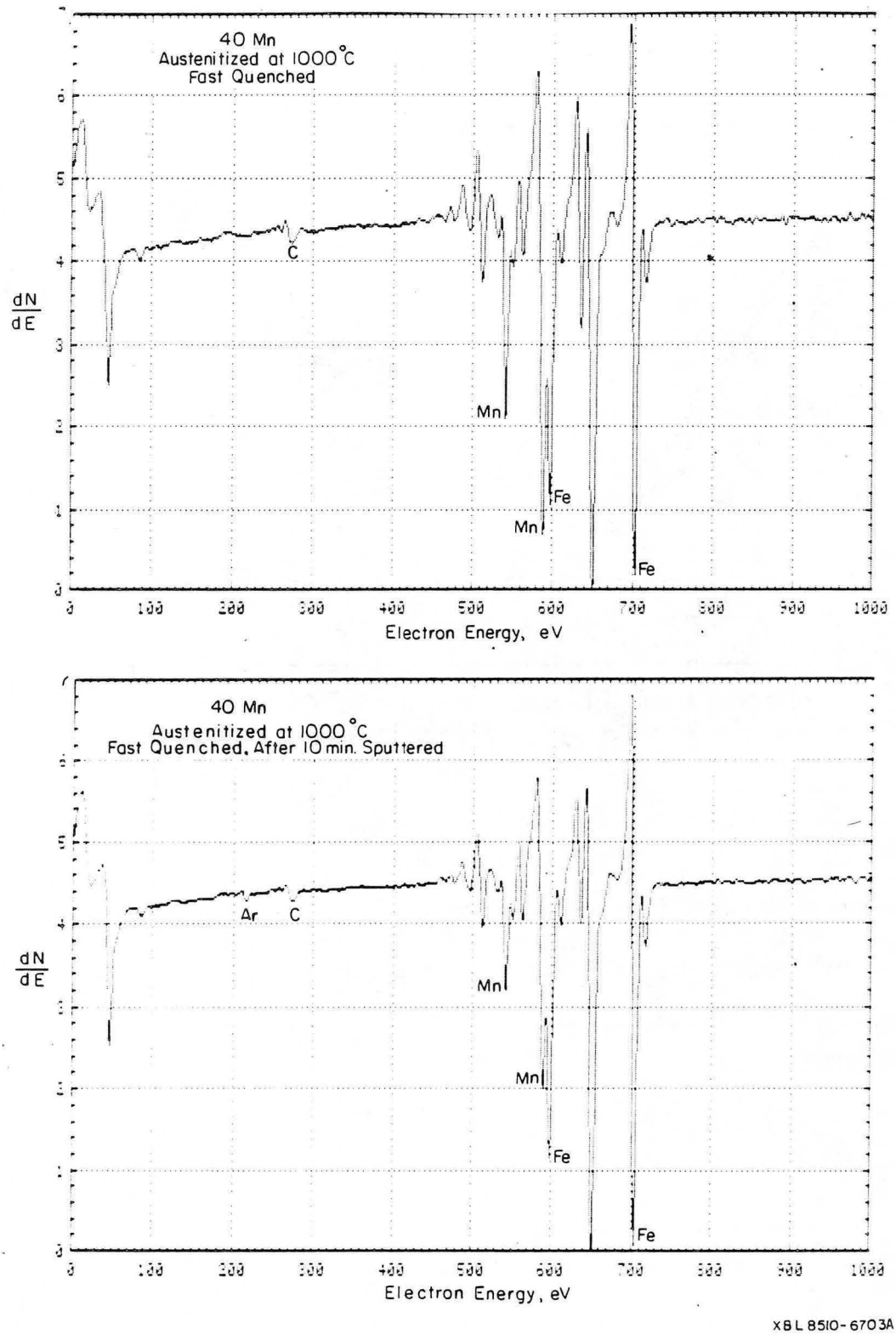
40 Mn
Austenitized at 1000°C
Fast Quenched
C
Mn
Fe
Mn
Fe
dN/dE
Electron Energy, eV
40 Mn
Austenitized at 1000°C
Fast Quenched, After 10 min. Sputtered
Ar
C
Mn
Mn
Fe
Fe
dN/dE
Electron Energy, eV
XBL 8510-6703A

Figure 16

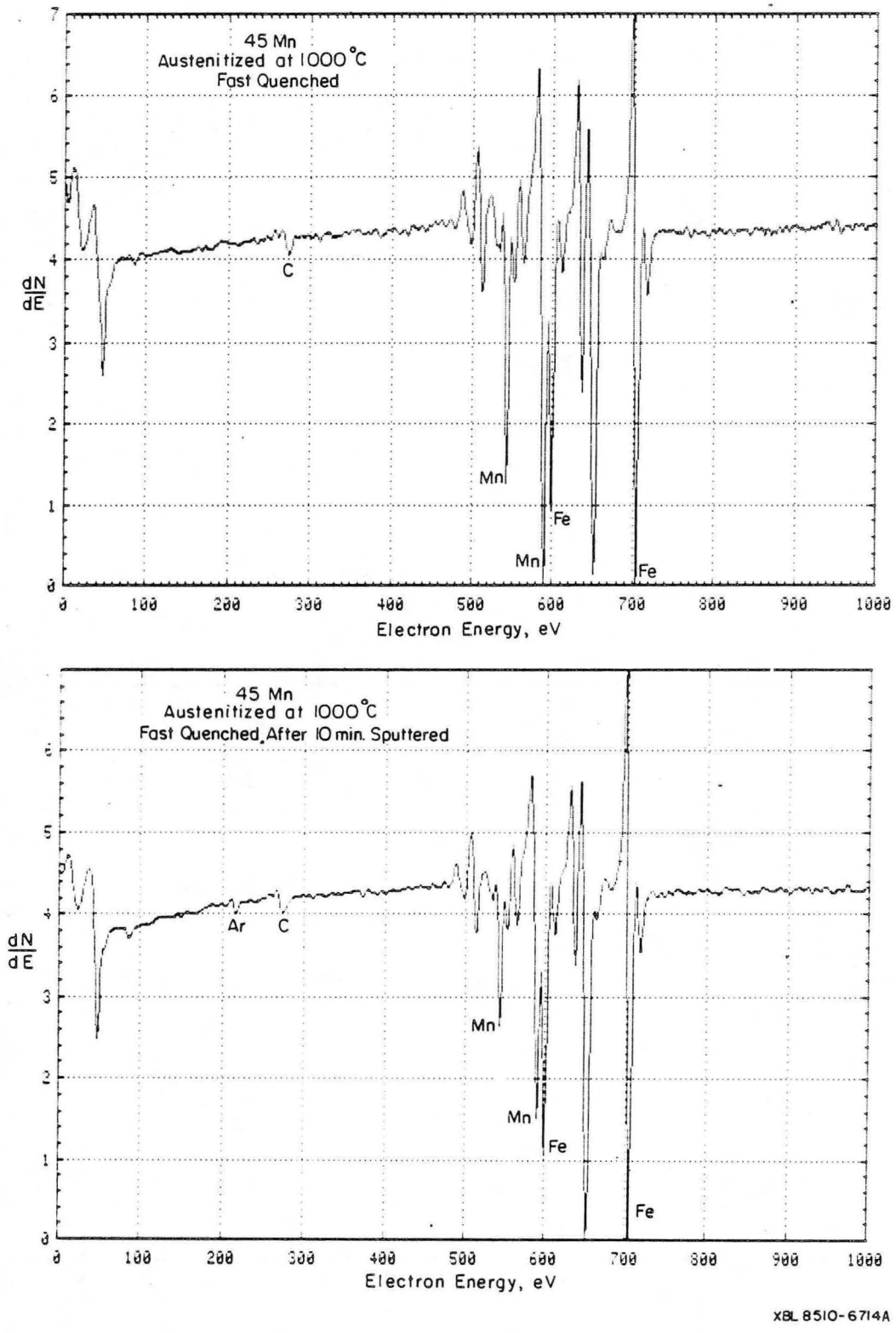
45 Mn
Austenitized at 1000°C
Fast Quenched
C
Mn
Fe
Mn
Fe
dN/dE
Electron Energy, eV
45 Mn
Austenitized at 1000°C
Fast Quenched, After 10 min. Sputtered
Ar
C
Mn
Mn
Fe
Fe
dN/dE
Electron Energy, eV
XBL 8510-6714A

Figure 17(a)

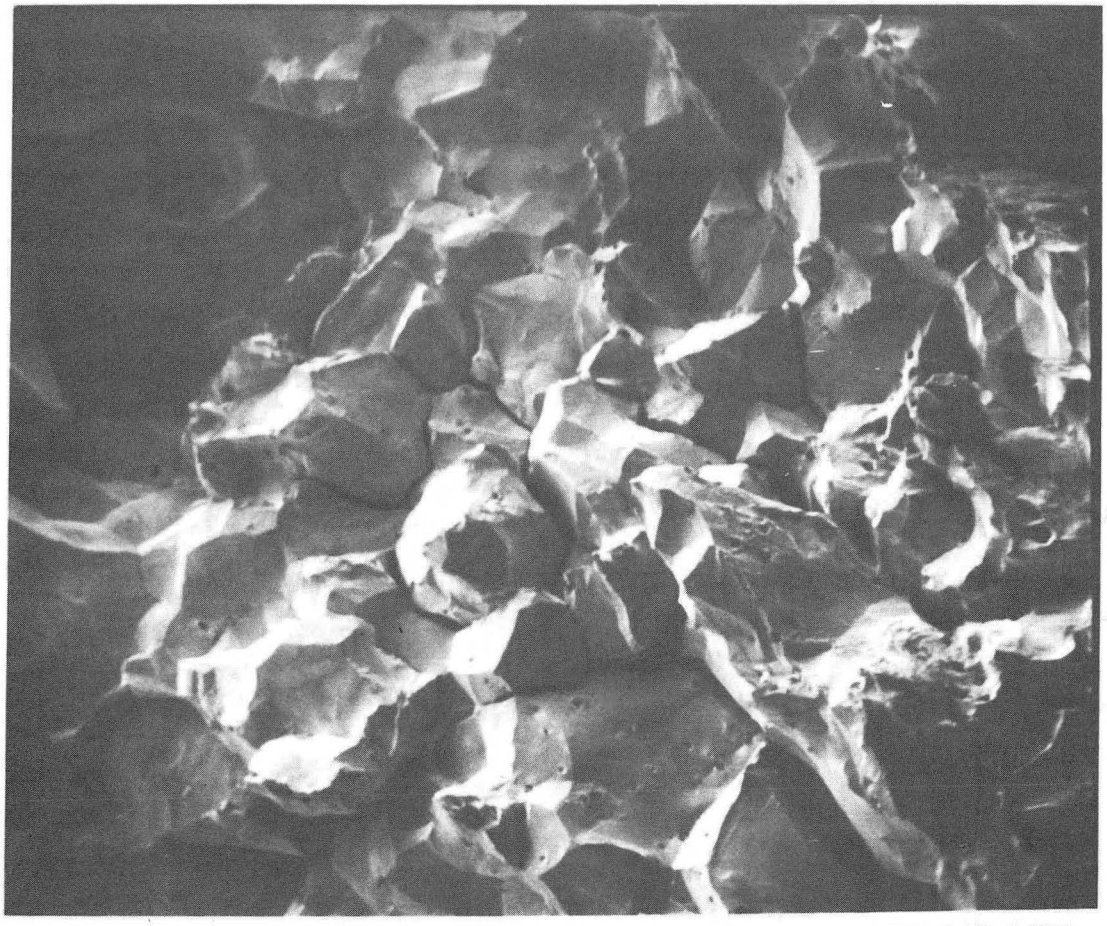

XBB 863-1680

Figure 17(b)

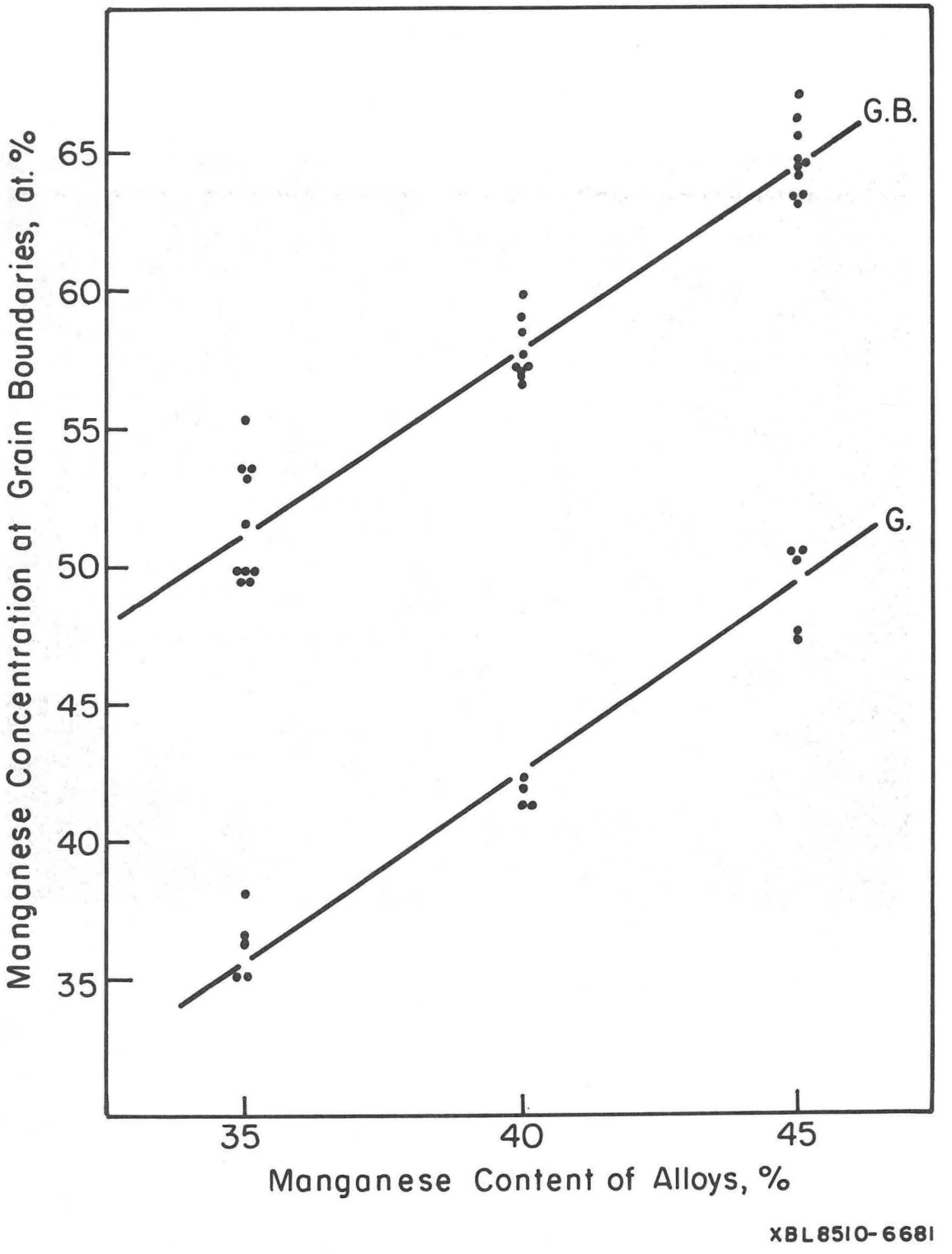
Manganese Concentration at Grain Boundaries, at.%
65
60
55
50
45
40
35
G.B.
G.
35
40
45
Manganese Content of Alloys, %
XBL8510-6681

Figure 18

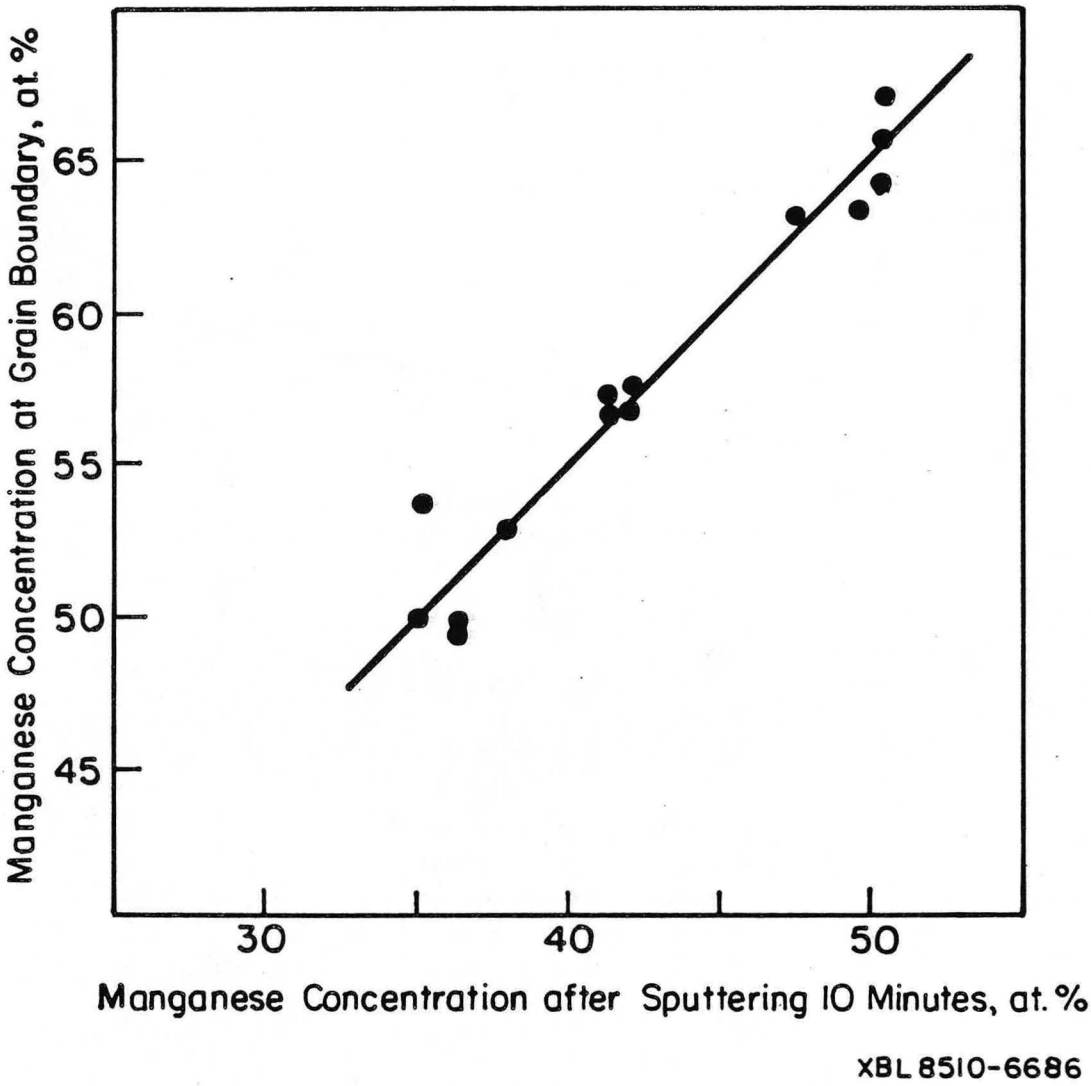
Manganese Concentration at Grain Boundary, at.%
65
60
55
50
45
30
40
50
Manganese Concentration after Sputtering 10 Minutes, at.%
XBL 8510-6686

Figure 19

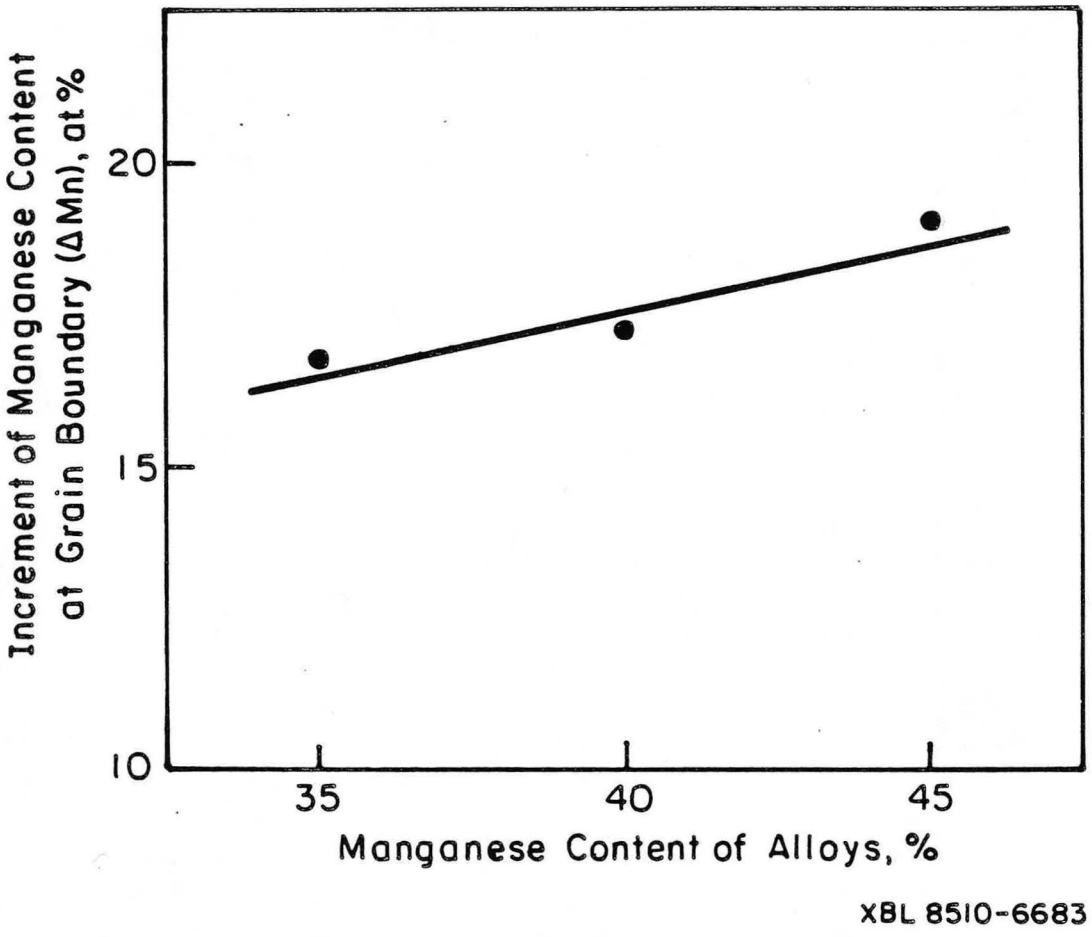
Increment of Manganese Content at Grain Boundary (ΔMn), at %
20
15
10
35
40
45
Manganese Content of Alloys, %
XBL 8510-6683

Figure 20

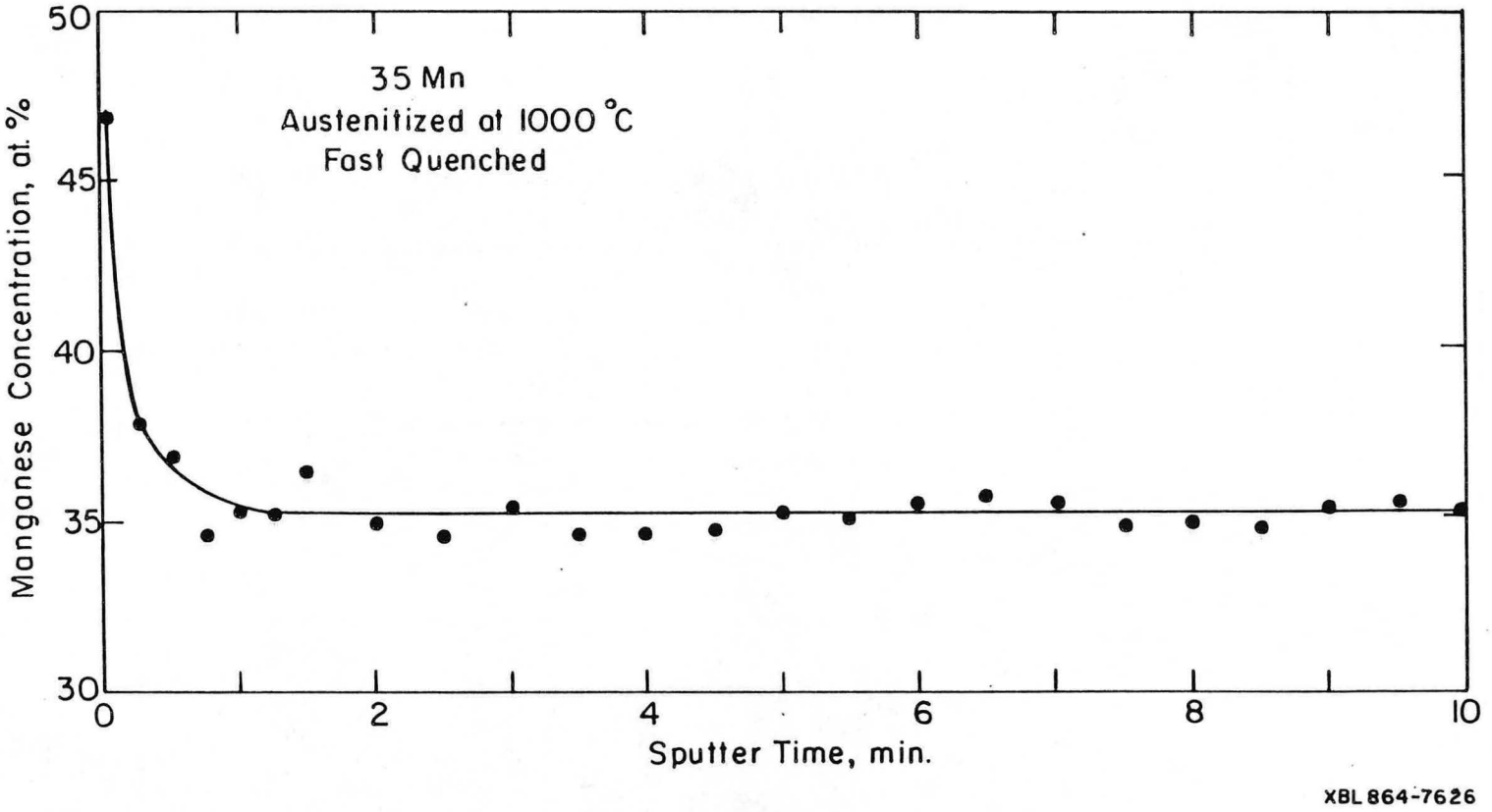
35 Mn
Austenitized at 1000 °C
Fast Quenched
Manganese Concentration, at. %
50
45
40
35
30
0
2
4
6
8
10
Sputter Time, min.
XBL 864-7626

Figure 21

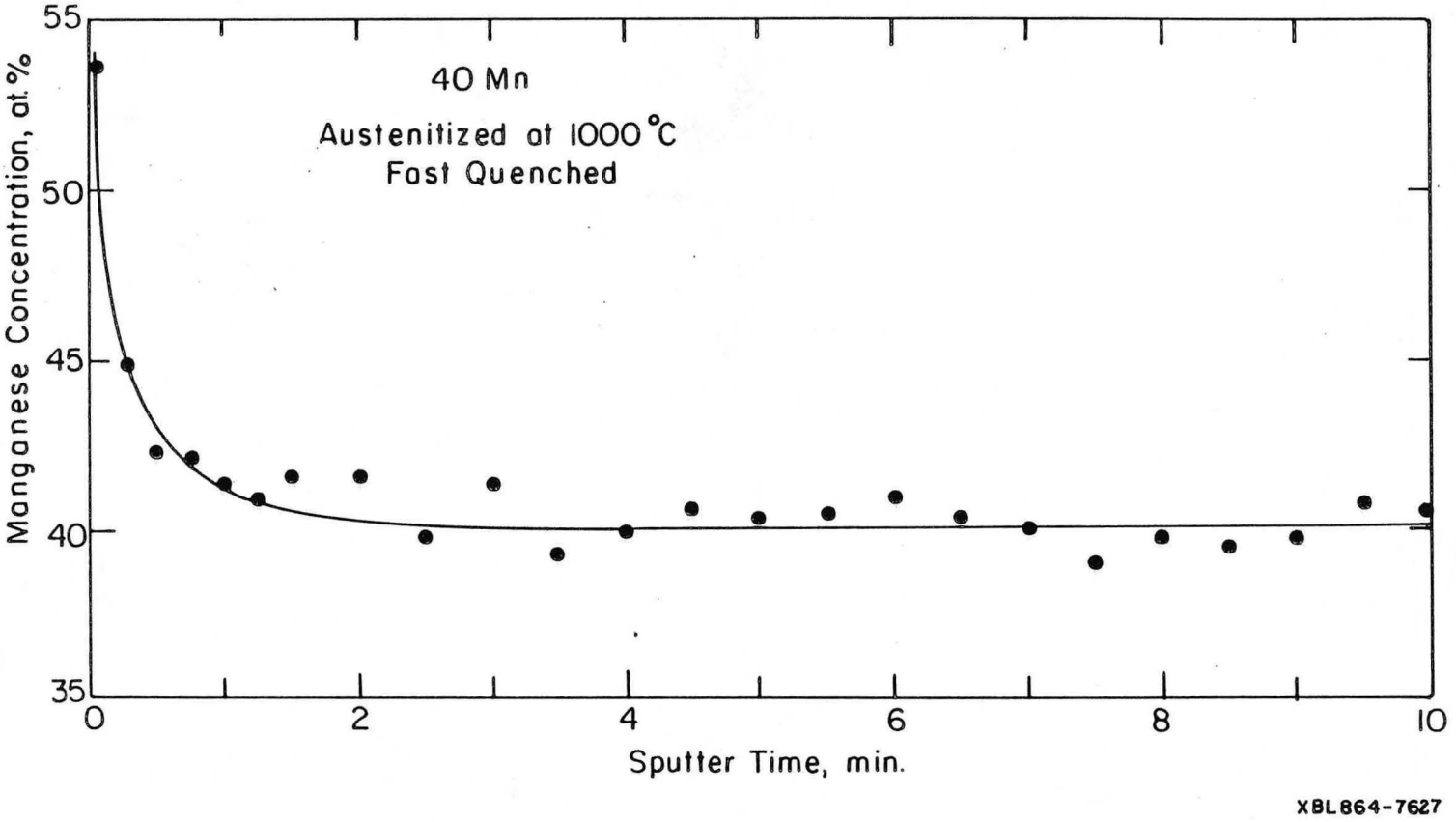
40 Mn
Austenitized at 1000 °C
Fast Quenched
Manganese Concentration, at.%
55
50
45
40
35
0
2
4
6
8
10
Sputter Time, min.
XBL864-7627

Figure 22

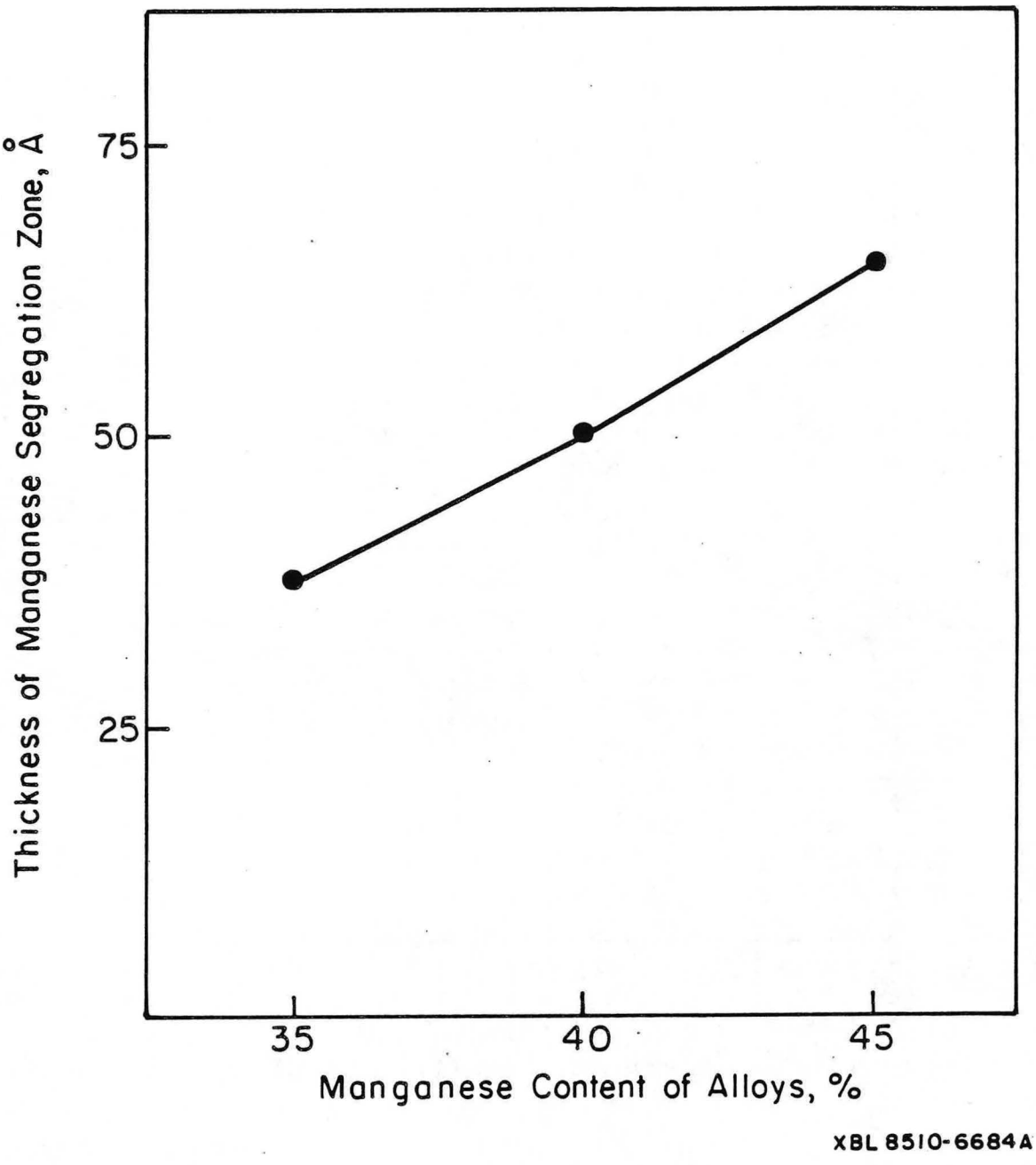
Thickness of Manganese Segregation Zone, Å
75
50
25
35
40
45
Manganese Content of Alloys, %
XBL 8510-6684A

Figure 23

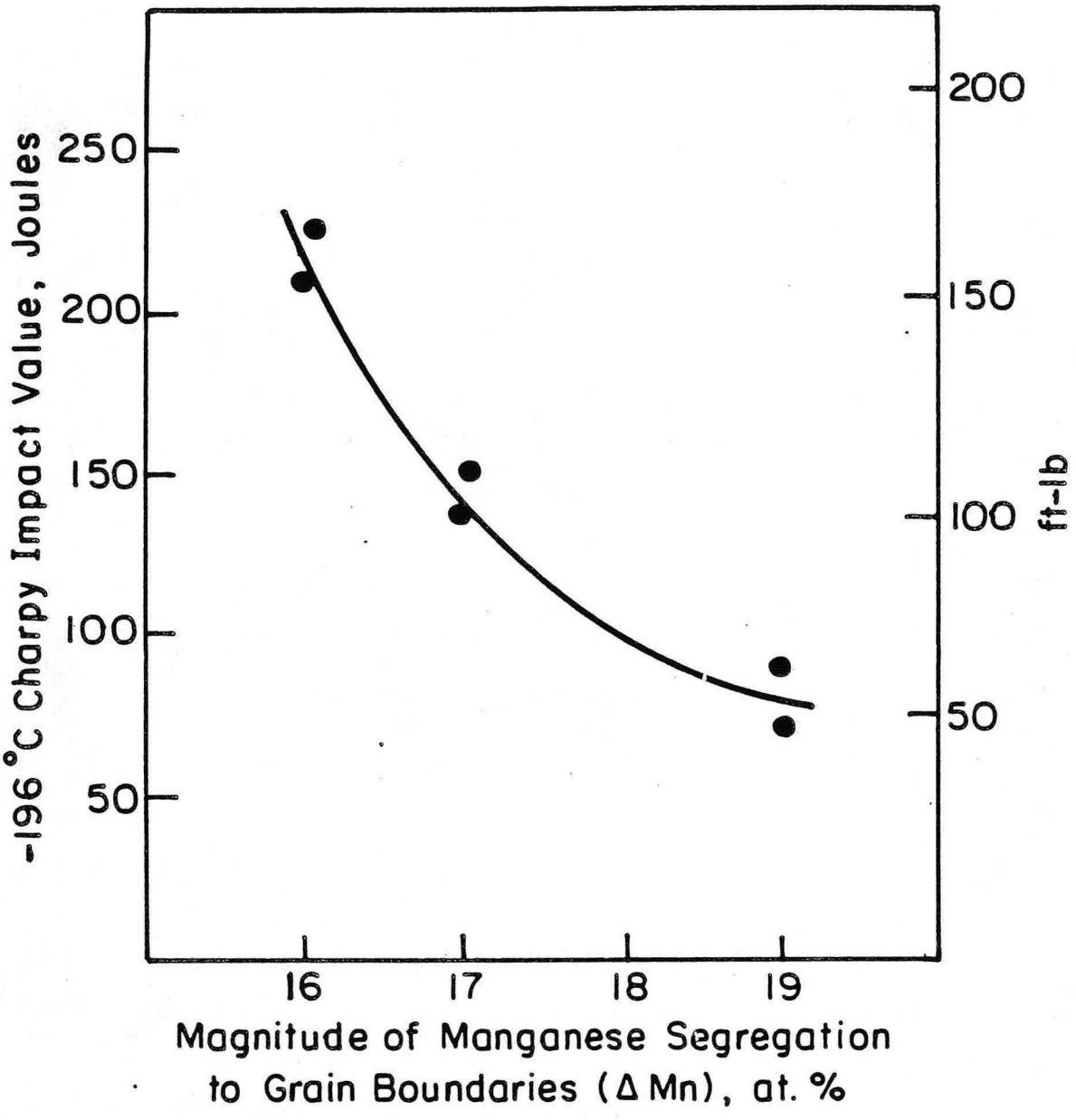

XBL 863-7563

Figure 24

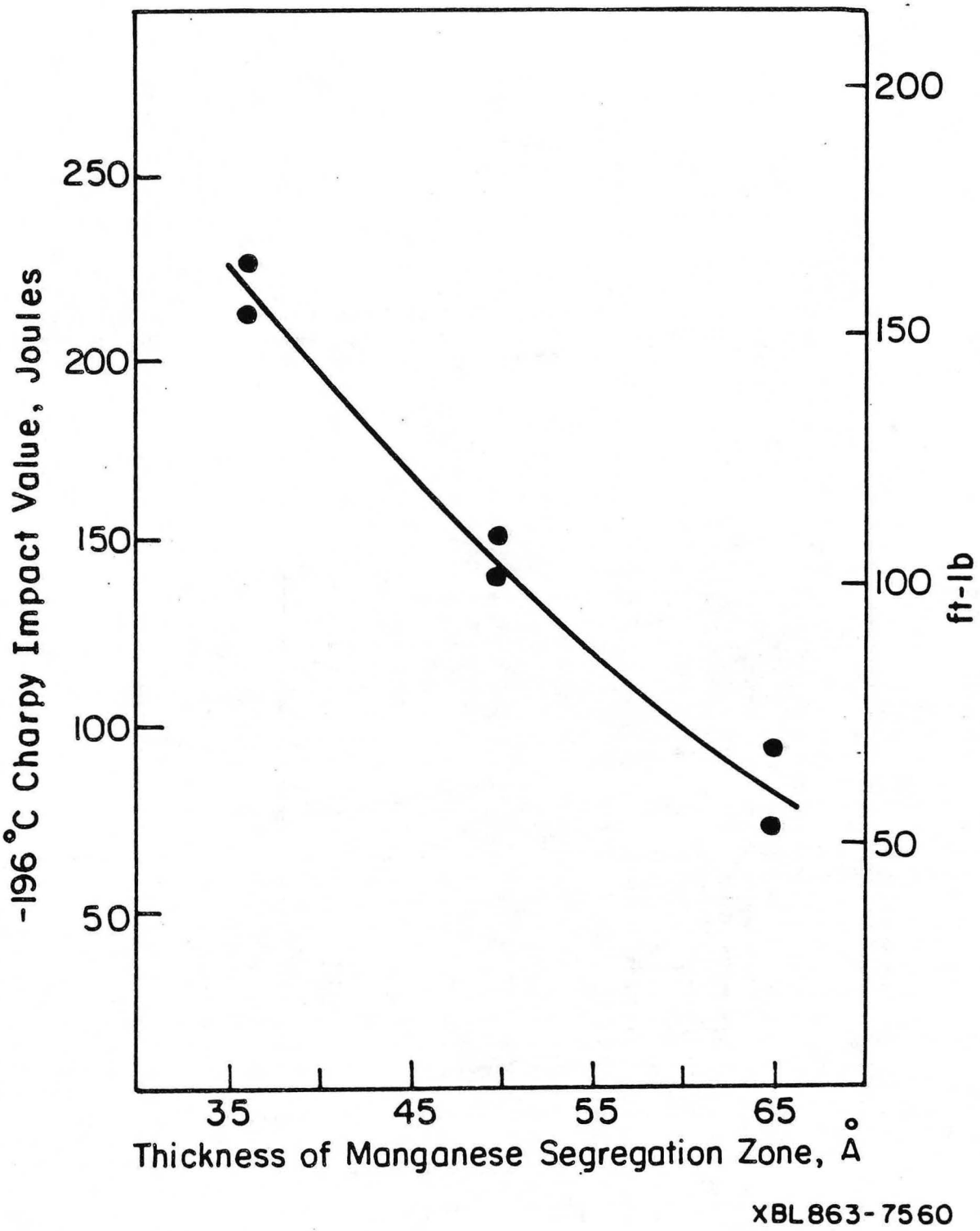
-196 °C Charpy Impact Value, Joules
250
200
150
100
50
200
150
100
50
ft-lb
35
45
55
65
Thickness of Manganese Segregation Zone, Å
XBL863-7560

Figure 25

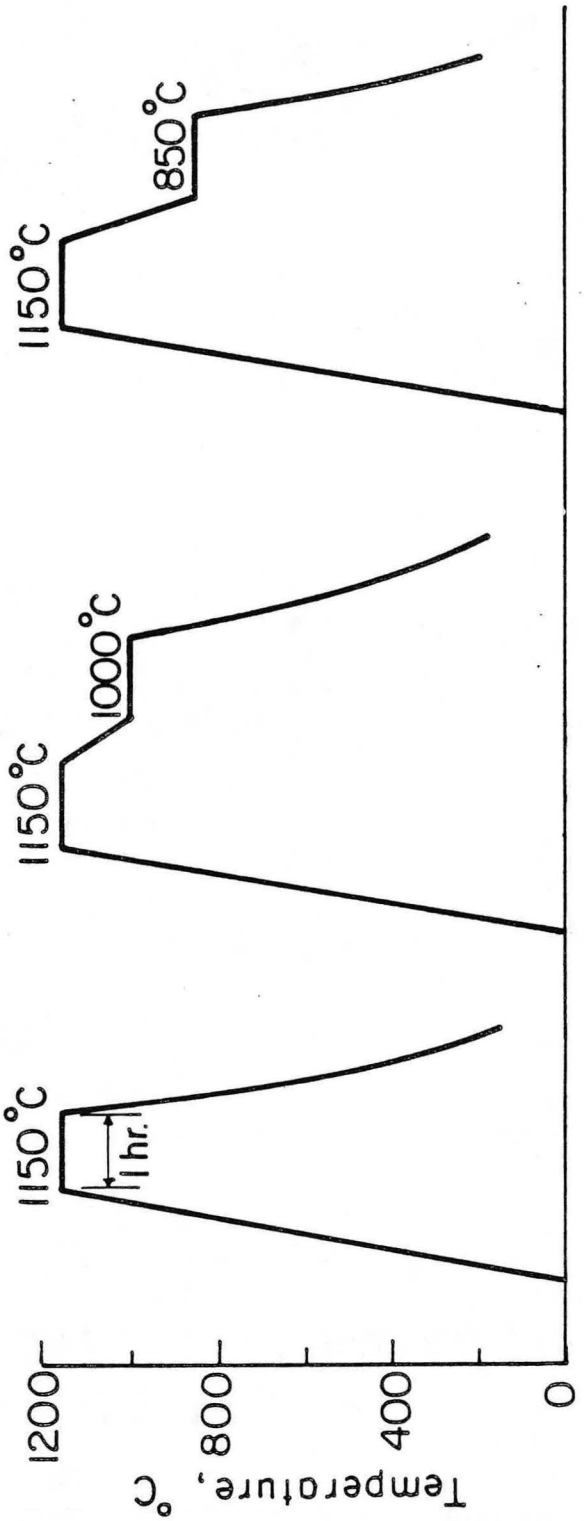
1150°C
1 hr.
1150°C
1000°C
1150°C
850°C
Time
Temperature, °C
1200
800
400
0
XBL 863-7558

Figure 26

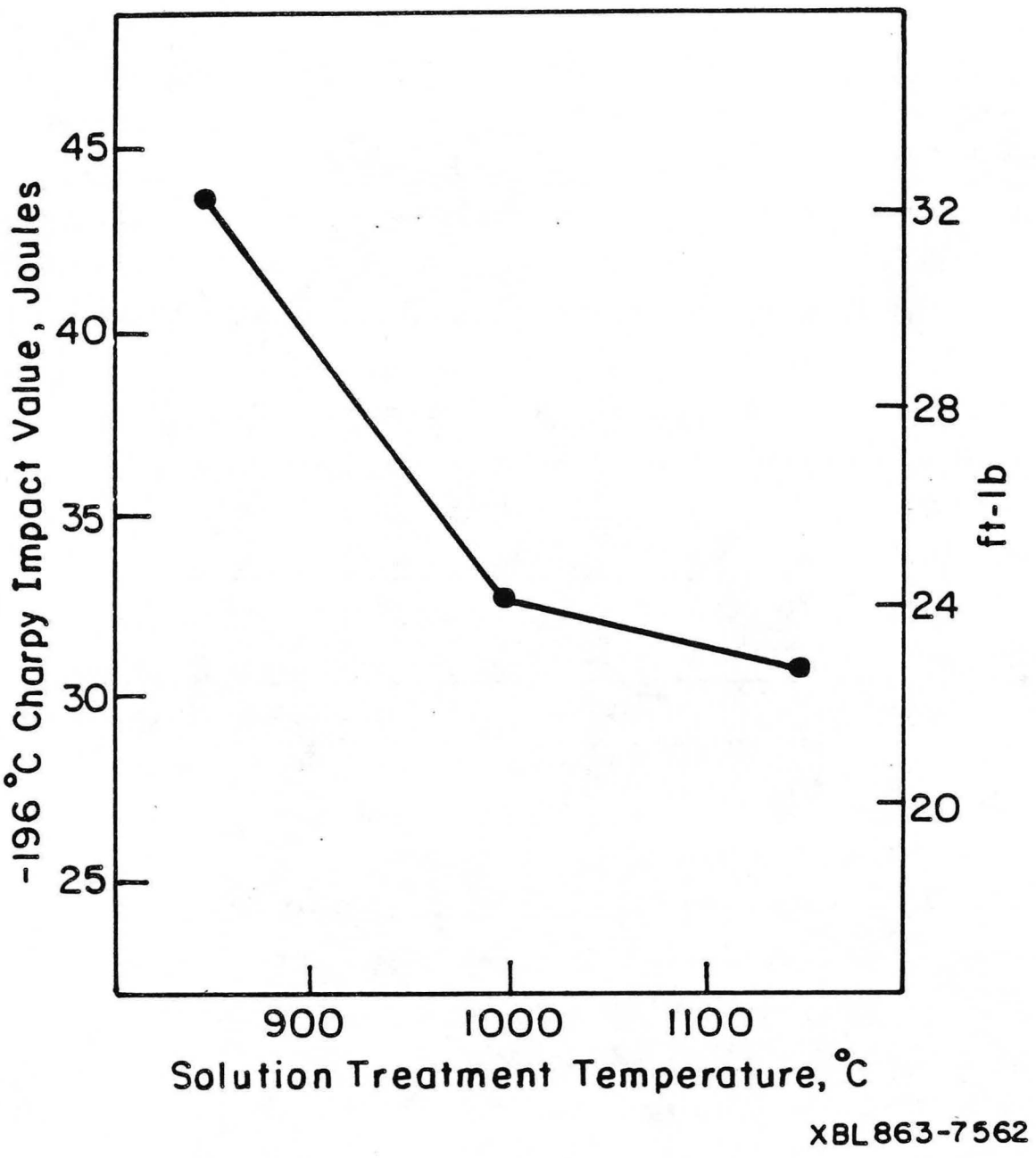
-196 °C Charpy Impact Value, Joules
45
40
35
30
25
32
28
24
20
ft-lb
900
1000
1100
Solution Treatment Temperature, °C
XBL863-7562

Figure 27

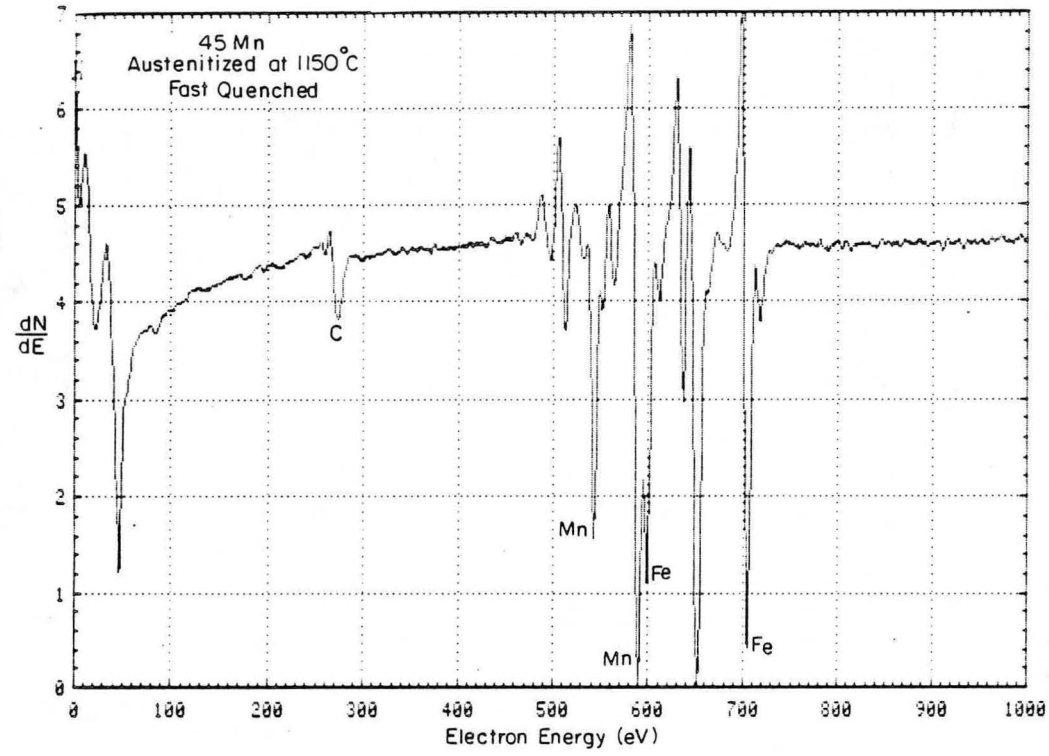

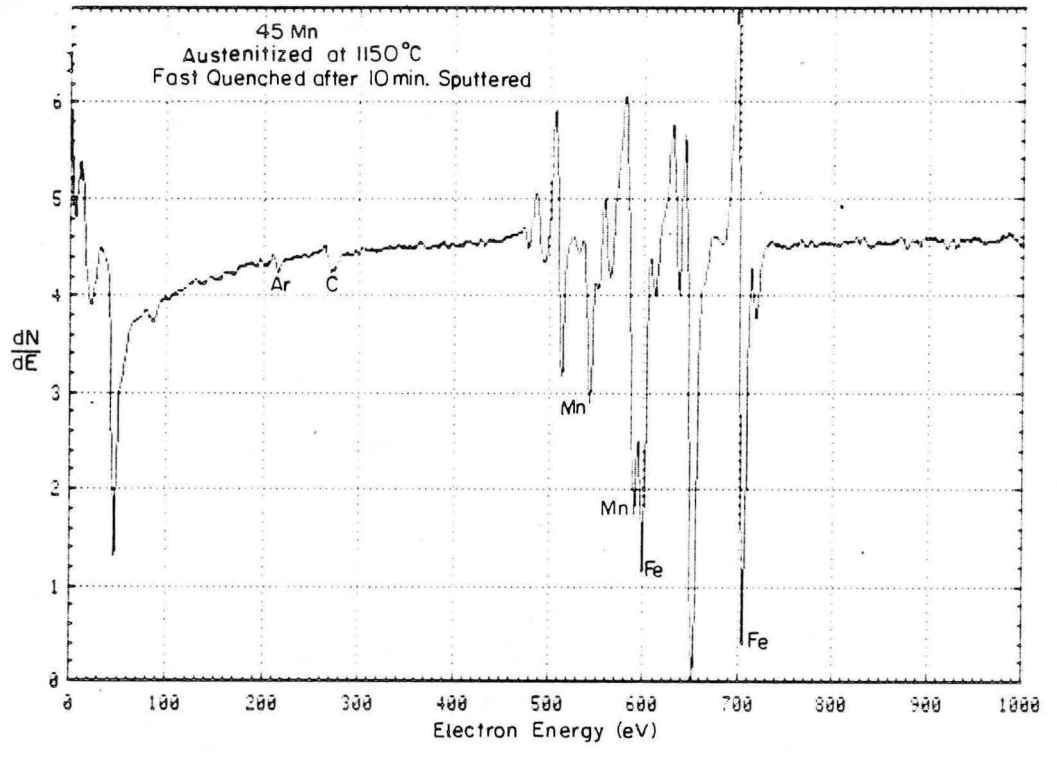

XBL8510-6738A

Figure 28(a)

XBB 863-1679

Figure 28(b)

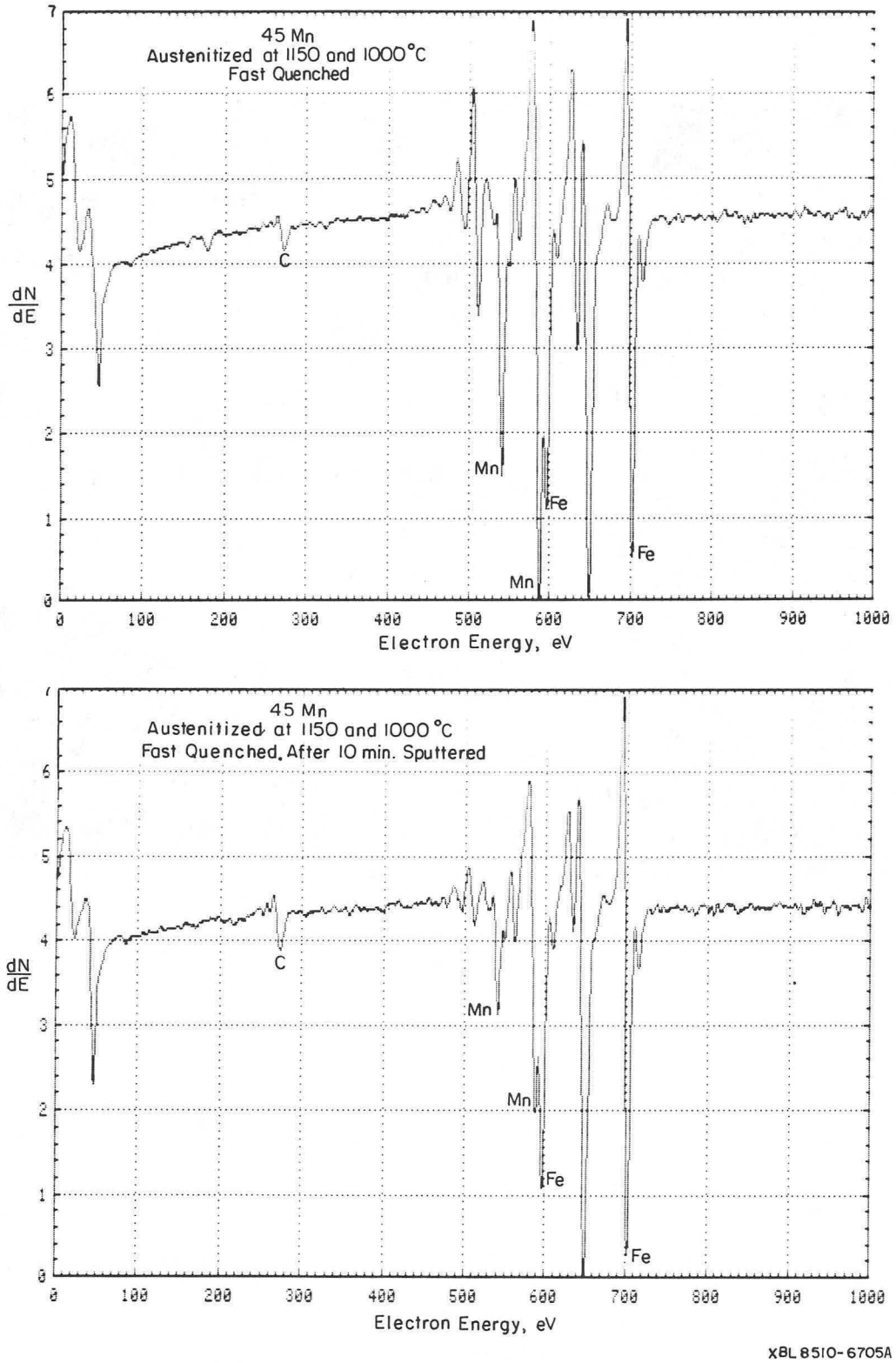
45 Mn
Austenitized at 1150 and 1000°C
Fast Quenched
dN/dE
C
Mn
Fe
Mn
Fe
Electron Energy, eV
45 Mn
Austenitized at 1150 and 1000 °C
Fast Quenched, After 10 min. Sputtered
dN/dE
C
Mn
Mn
Fe
Fe
Electron Energy, eV
XBL 8510-6705A

Figure 29(a)

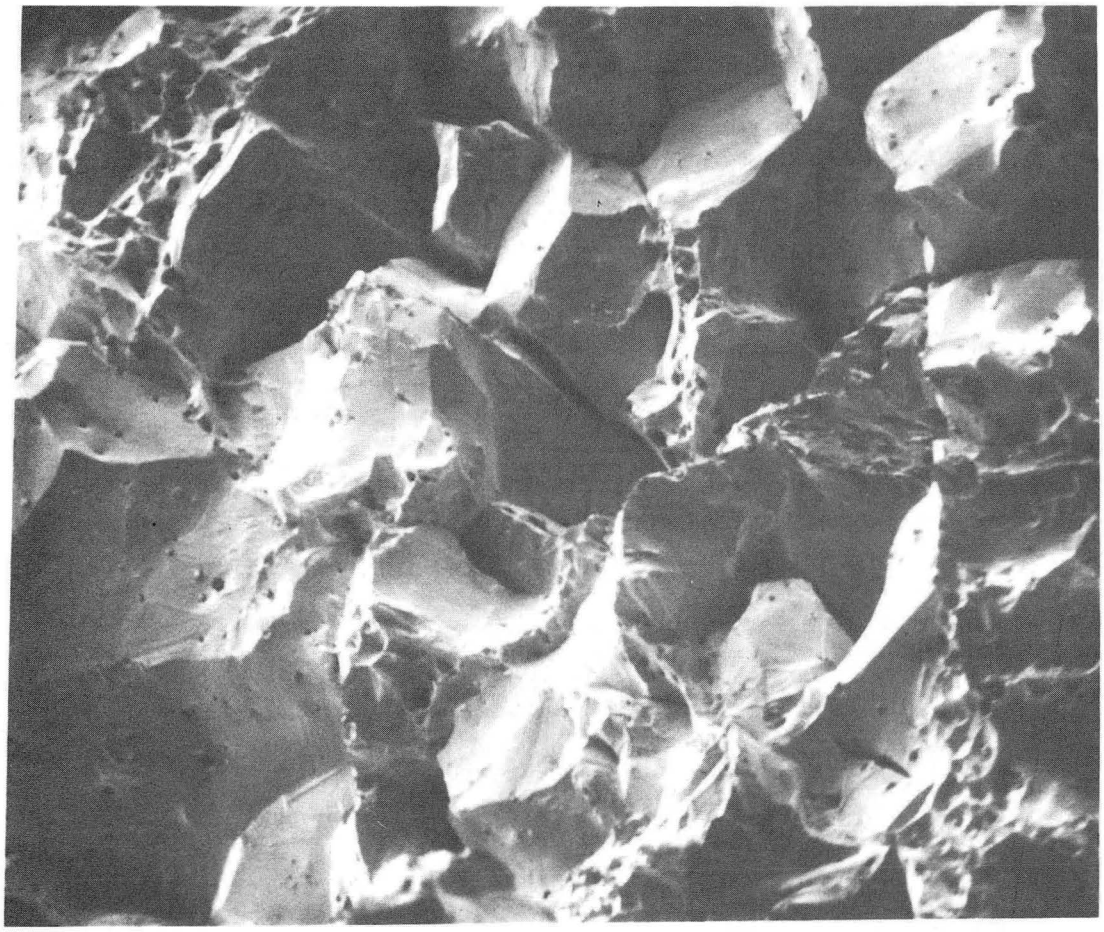

XBB 863-1678

Figure 29(b)

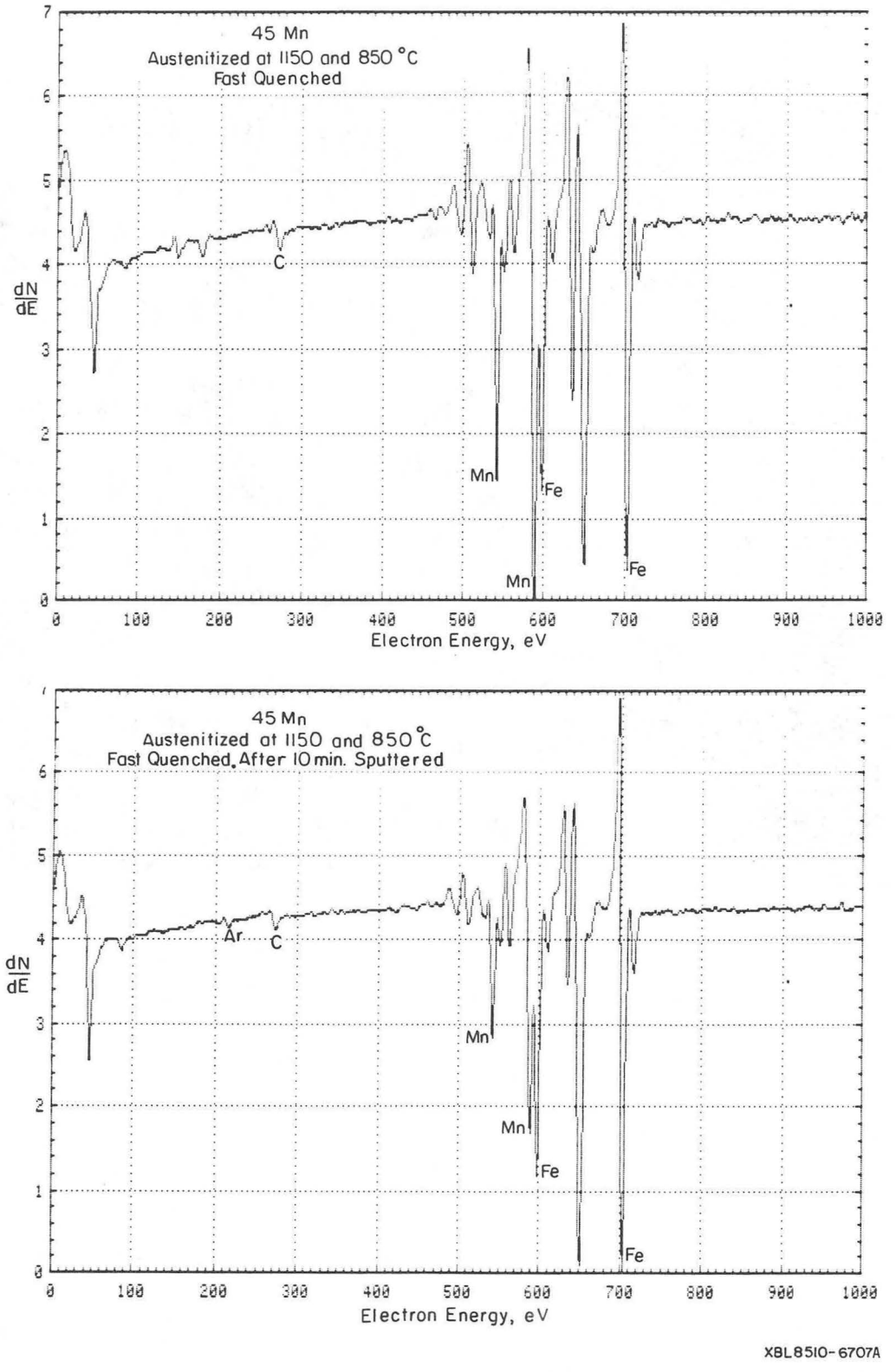
45 Mn
Austenitized at 1150 and 850 °C
Fast Quenched
C
Mn
Fe
Mn
Fe
dN/dE
Electron Energy, eV
45 Mn
Austenitized at 1150 and 850 °C
Fast Quenched, After 10 min. Sputtered
Ar
C
Mn
Mn
Fe
Fe
dN/dE
Electron Energy, eV
XBL8510-6707A

Figure 30(a)

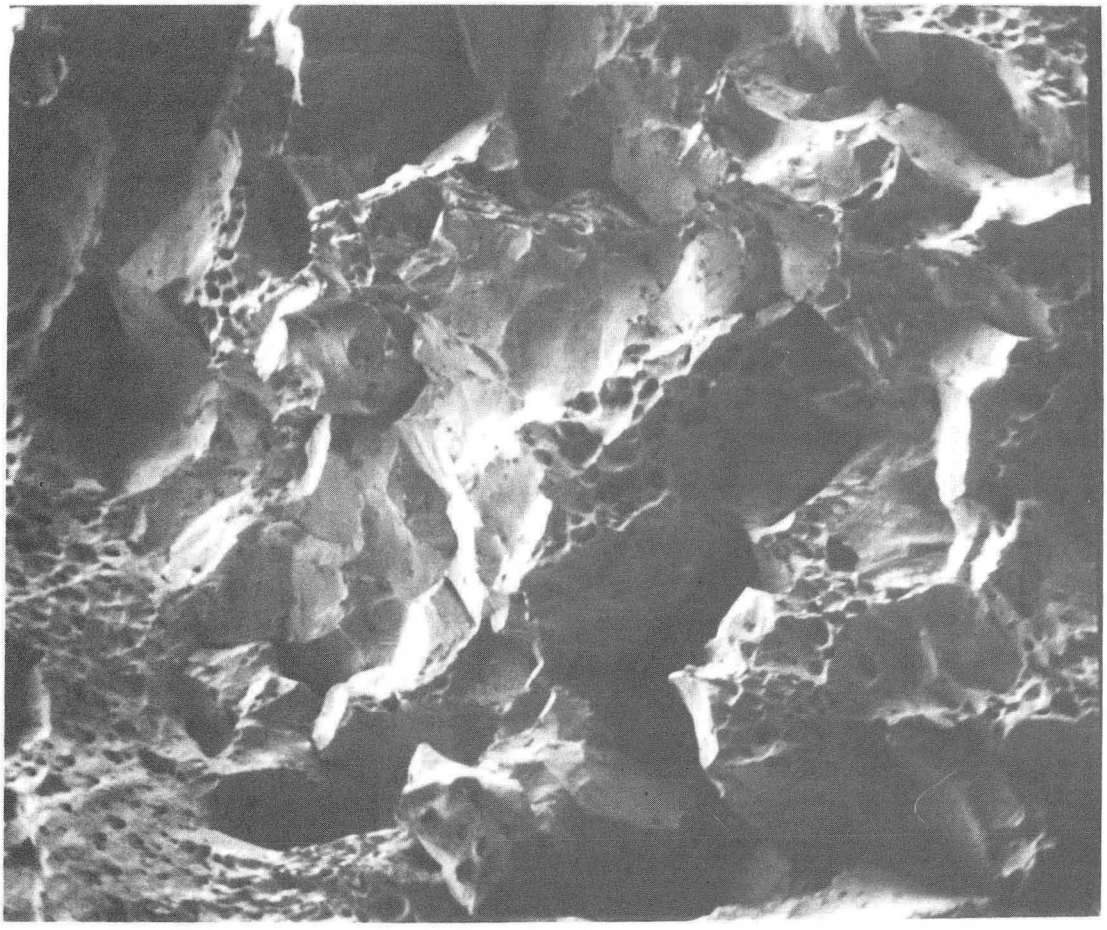

XBB 863-1677

Figure 30(b)

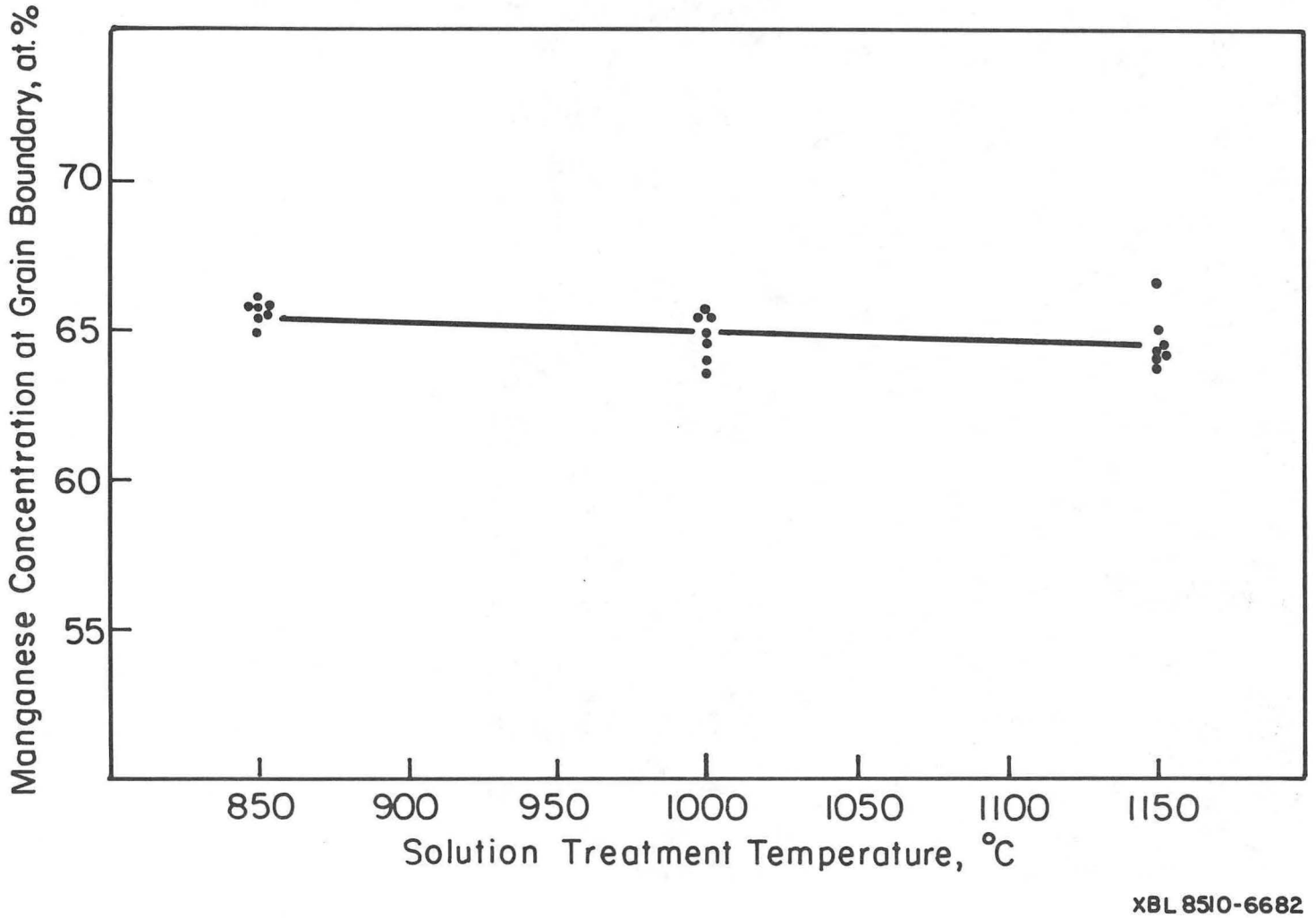
Manganese Concentration at Grain Boundary, at.%
70
65
60
55
850
900
950
1000
1050
1100
1150
Solution Treatment Temperature, °C
XBL 8510-6682

Figure 31

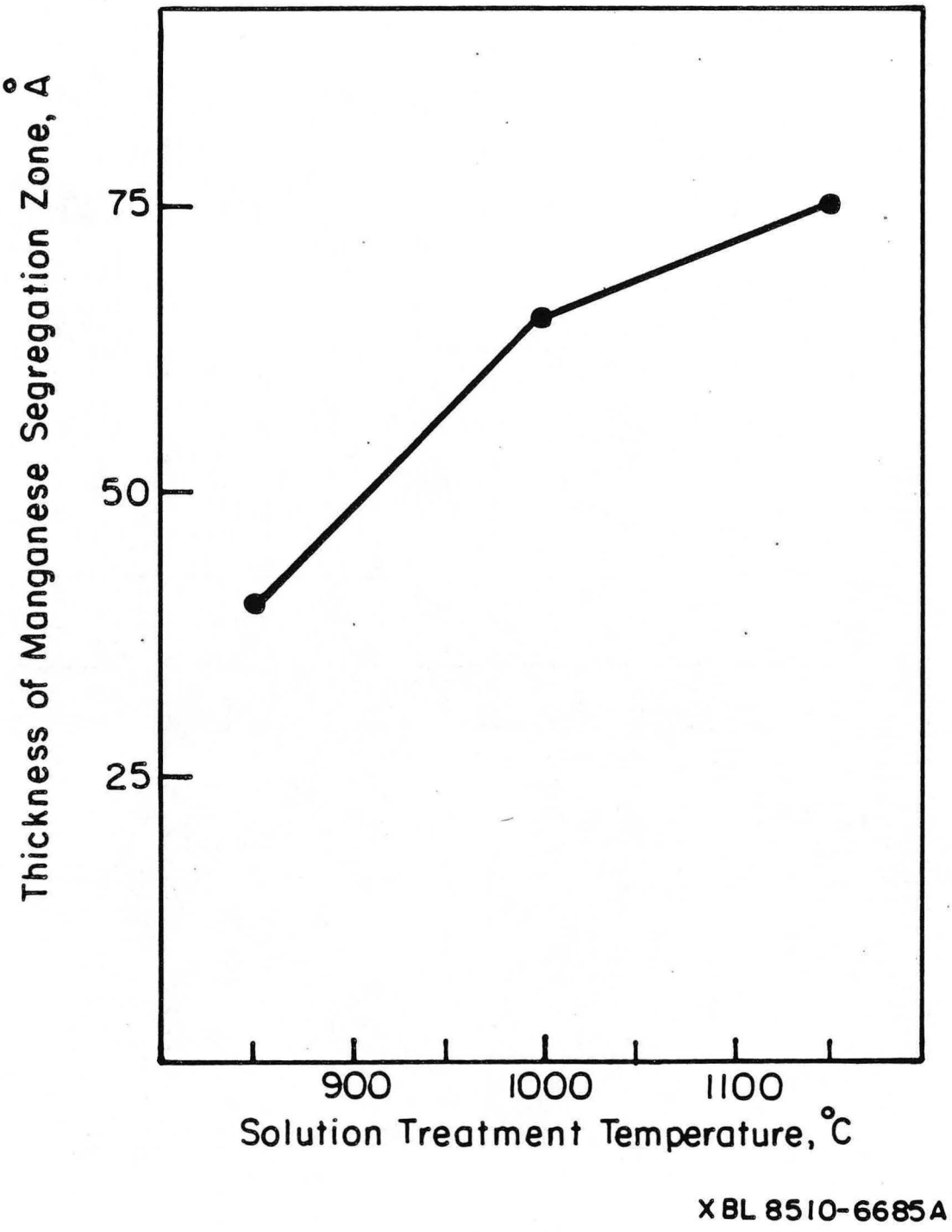
Thickness of Manganese Segregation Zone, Å
75
50
25
900
1000
1100
Solution Treatment Temperature, °C
XBL 8510-6685A

Figure 32

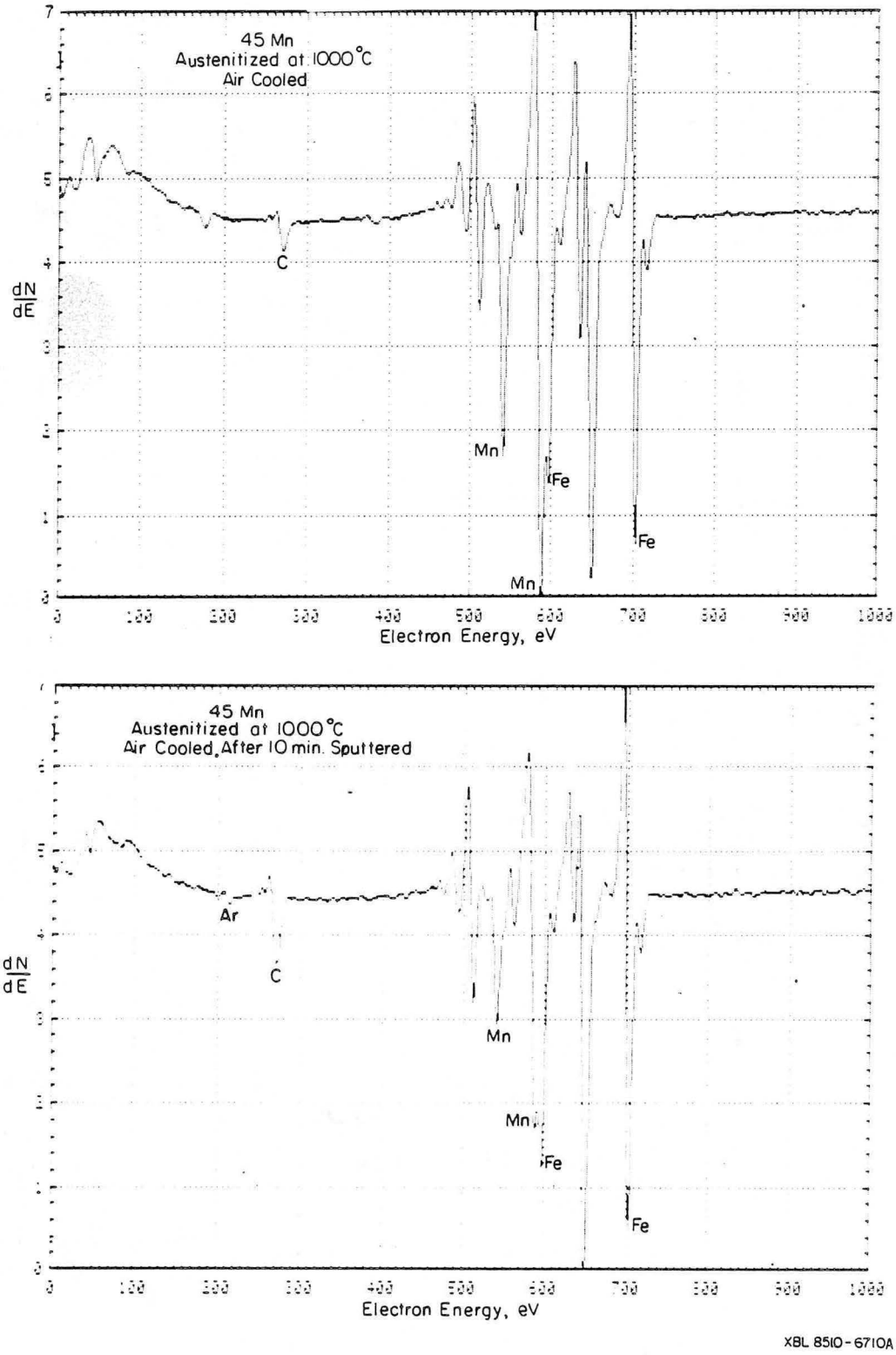
45 Mn
Austenitized at 1000°C
Air Cooled
C
Mn
Fe
Mn
Fe
dN/dE
Electron Energy, eV
45 Mn
Austenitized at 1000°C
Air Cooled, After 10 min. Sputtered
Ar
C
Mn
Mn
Fe
Fe
dN/dE
Electron Energy, eV
XBL 8510-6710A

Figure 33(a)

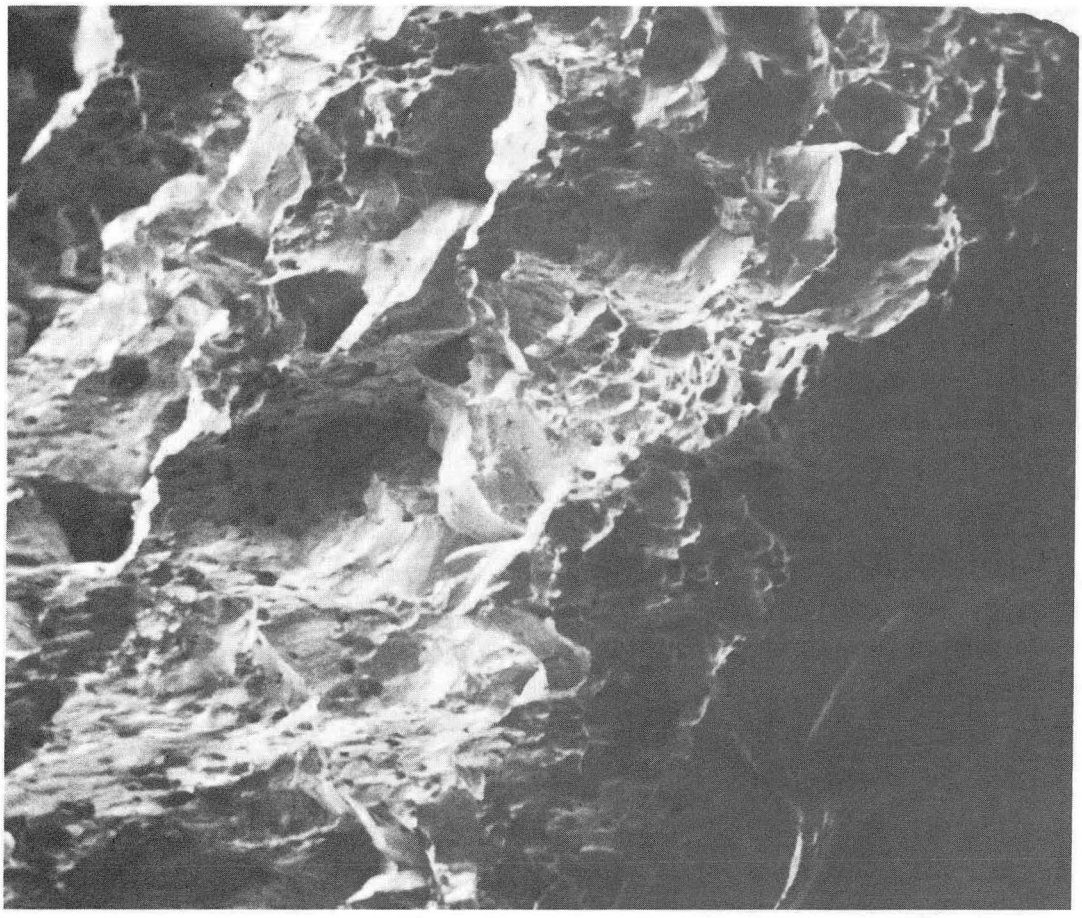

XBB 863-1675

Figure 33(b)

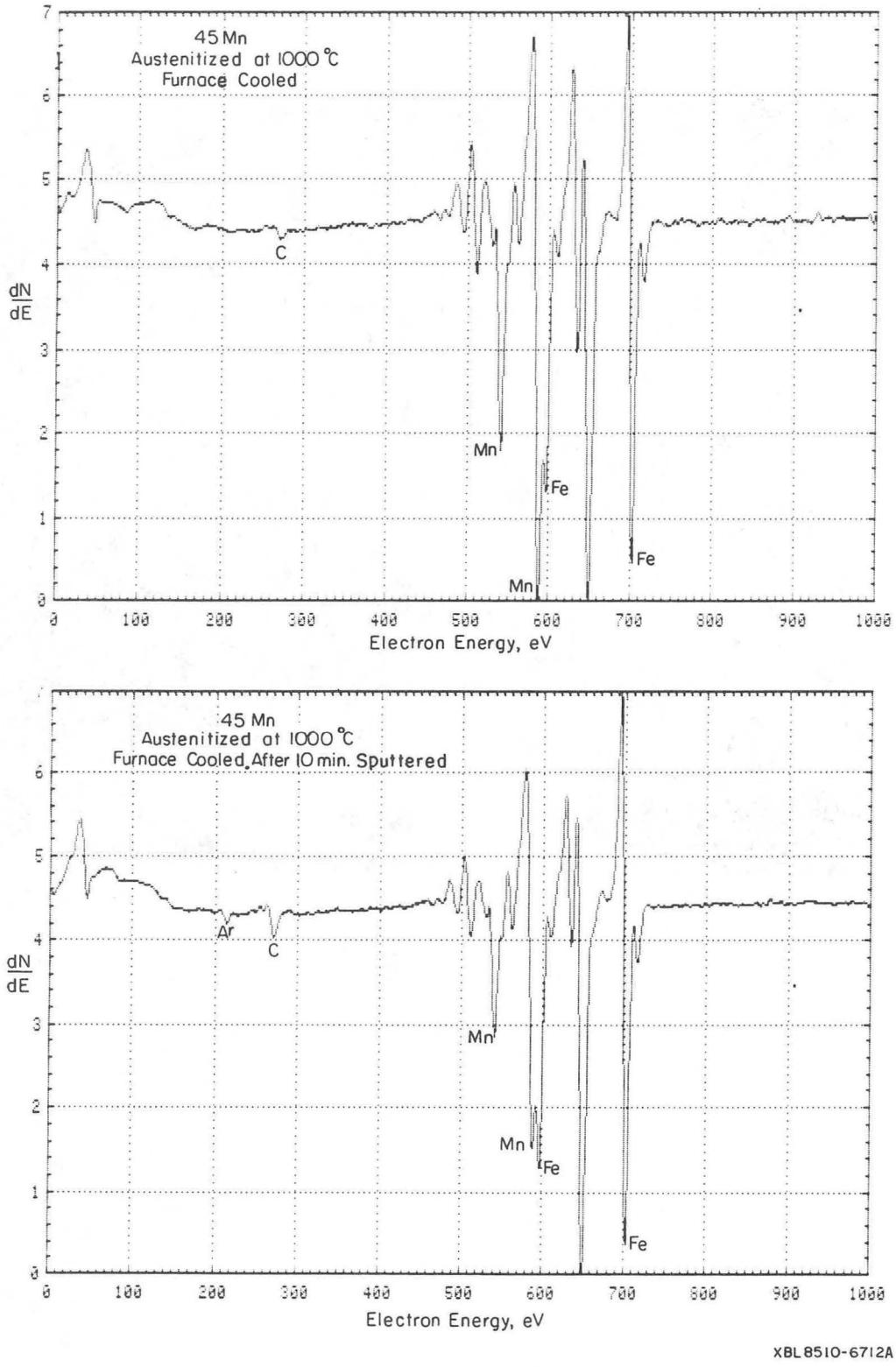
45 Mn
Austenitized at 1000 °C
Furnace Cooled
C
Mn
Fe
Mn
Fe
dN/dE
Electron Energy, eV
45 Mn
Austenitized at 1000 °C
Furnace Cooled, After 10 min. Sputtered
Ar
C
Mn
Mn
Fe
Fe
dN/dE
Electron Energy, eV
XBL8510-6712A

Figure 34(a)

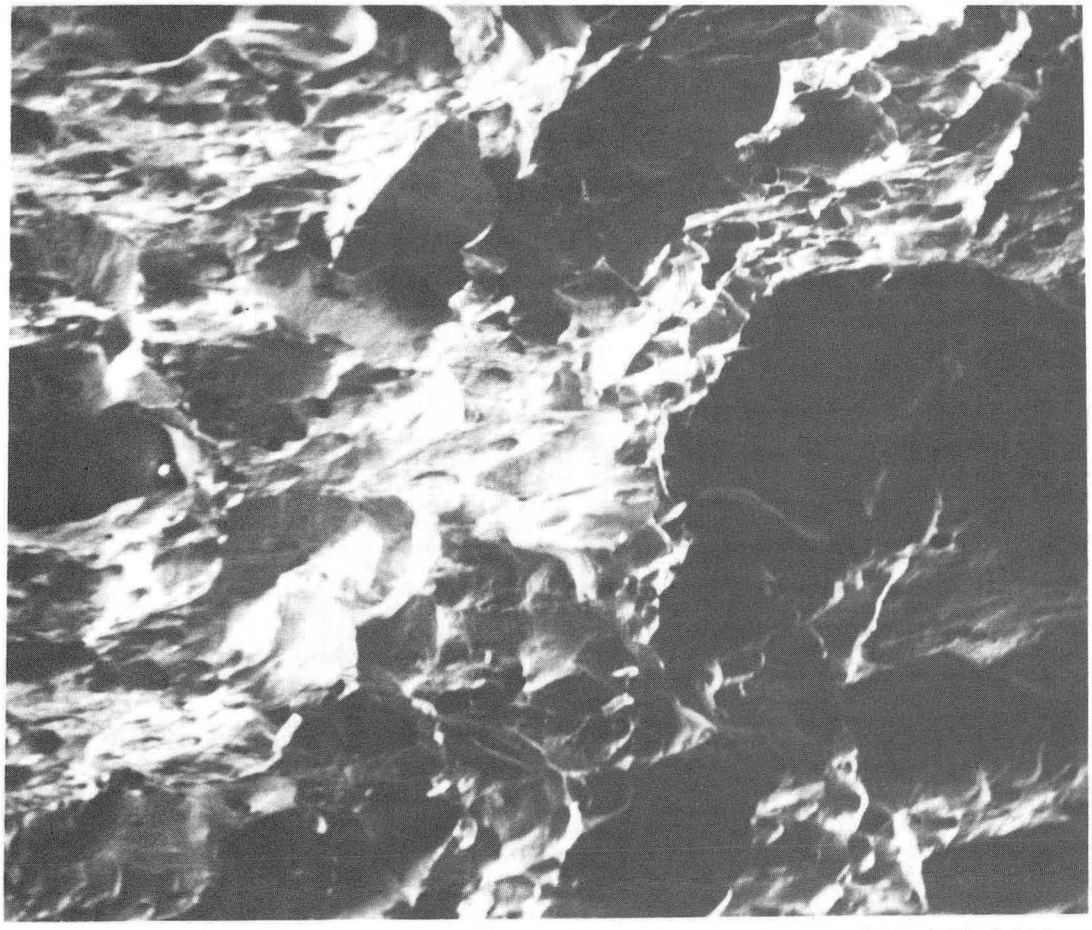

XBB 863-1676

Figure 34(b)

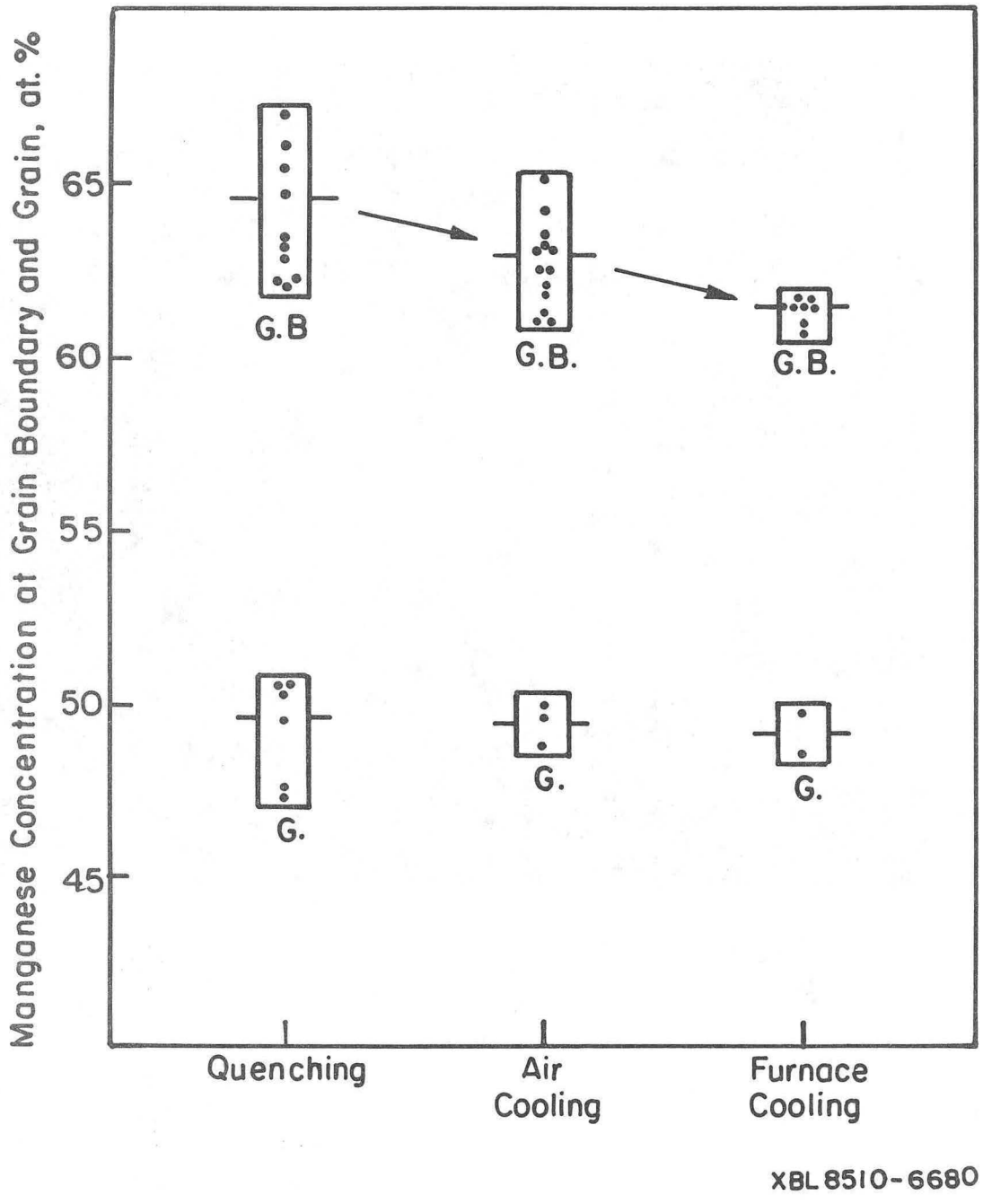
Manganese Concentration at Grain Boundary and Grain, at.%
65
60
55
50
45
G.B
G.B.
G.B.
G.
G.
G.
Quenching
Air Cooling
Furnace Cooling
XBL 8510-6680

Figure 35

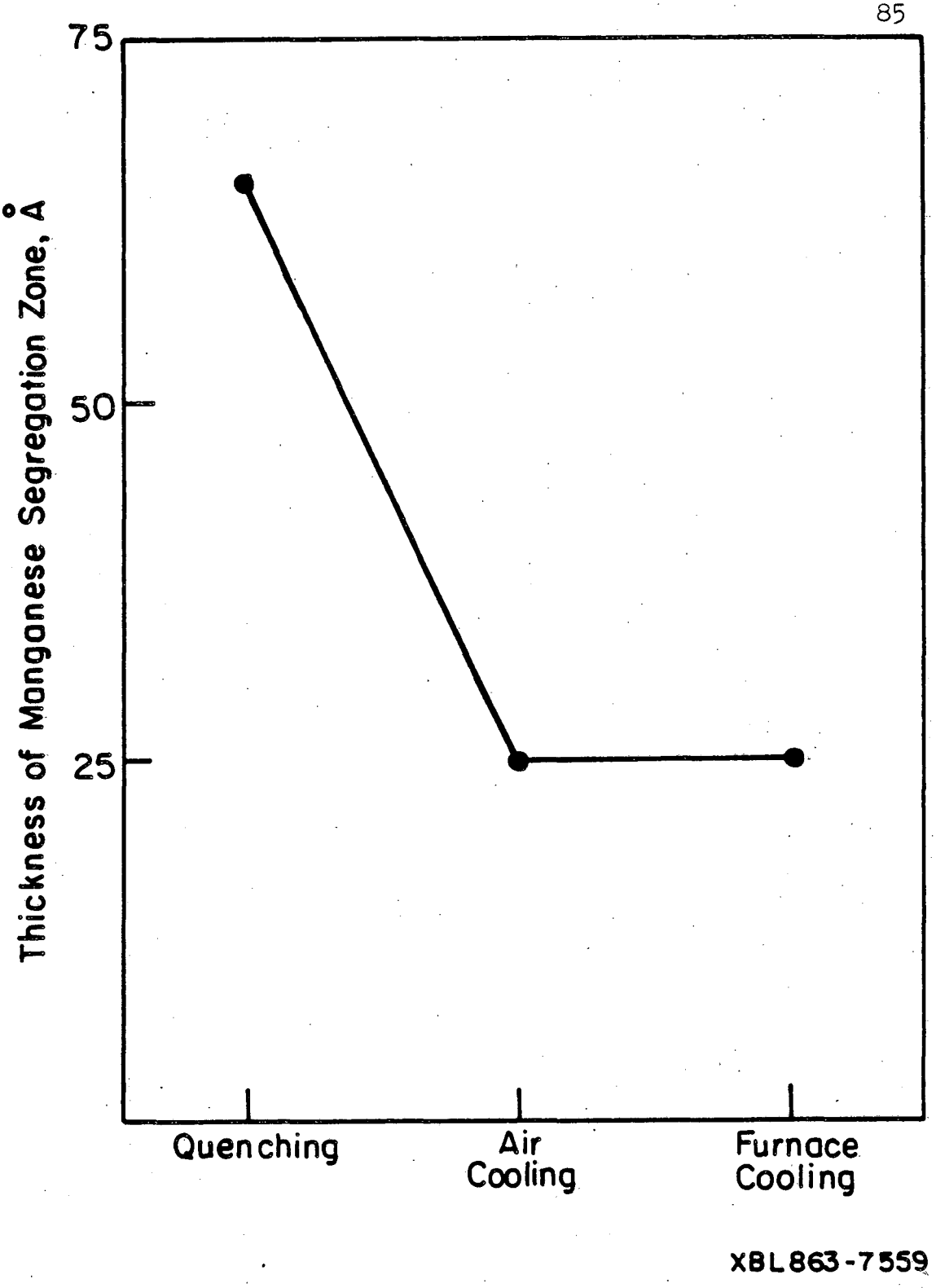
75
50
25
Thickness of Manganese Segregation Zone, Å
Quenching
Air Cooling
Furnace Cooling
XBL863-7559

Figure 36

LAWRENCE BERKELEY LABORATORY
TECHNICAL INFORMATION DEPARTMENT
UNIVERSITY OF CALIFORNIA
BERKELEY, CALIFORNIA 94720